©2020 Society of Economic Geologists, Inc.
*Economic Geology*, v. 115, no. 7, pp. 1443–1459

# A Continuum from Iron Oxide Copper-Gold to Iron Oxide-Apatite Deposits: Evidence from Fe and O Stable Isotopes and Trace Element Chemistry of Magnetite

Maria A. Rodriguez-Mustafa,[1,†] Adam C. Simon,[1] Irene del Real,[2,3,*] John F.H. Thompson,[4] Laura D. Bilenker,[5] Fernando Barra,[3,6] Ilya Bindeman,[7] and David Cadwell[8]

[1]*Department of Earth and Environmental Sciences, University of Michigan, 1100 North University Avenue, Ann Arbor, Michigan 48109-1005, USA*

[2]*Department of Earth and Atmospheric Sciences, Cornell University, 112 Hollister Drive, Ithaca, New York 14853-1504, USA*

[3]*Millennium Nucleus for Metal Tracing Along Subduction, Faculty of Physical and Mathematical Sciences (FCFM), Universidad de Chile, Santiago 8380450, Chile*

[4]*PetraScience Consultants, 3995 West 24th Avenue, Vancouver, British Columbia V6S 1M1, Canada*

[5]*Department of Geosciences, College of Sciences and Mathematics, Auburn University, 2050 Beard Eaves Memorial Coliseum, Auburn, Alabama 36849, USA*

[6]*Department of Geology and Andean Geothermal Center of Excellence (CEGA), Faculty of Physical and Mathematical Sciences (FCFM), Universidad de Chile, Plaza Ercilla 803, Santiago 8380450, Chile*

[7]*Department of Geological Sciences, University of Oregon, 1275 East 13th Avenue, Eugene, Oregon 97403-1272, USA*

[8]*215 Patee Canyon Drive, Missoula, Montana 59803-1626, USA*

## Abstract

Iron oxide copper-gold (IOCG) and iron oxide-apatite (IOA) deposits are major sources of Fe, Cu, and Au. Magnetite is the modally dominant and commodity mineral in IOA deposits, whereas magnetite and hematite are predominant in IOCG deposits, with copper sulfides being the primary commodity minerals. It is generally accepted that IOCG deposits formed by hydrothermal processes, but there is a lack of consensus for the source of the ore fluid(s). There are multiple competing hypotheses for the formation of IOA deposits, with models that range from purely magmatic to purely hydrothermal. In the Chilean iron belt, the spatial and temporal association of IOCG and IOA deposits has led to the hypothesis that IOA and IOCG deposits are genetically connected, where S-Cu-Au–poor magnetite-dominated IOA deposits represent the stratigraphically deeper levels of S-Cu-Au–rich magnetite- and hematite-dominated IOCG deposits. Here we report minor element and Fe and O stable isotope abundances for magnetite and H stable isotope abundances for actinolite from the Candelaria IOCG deposit and Quince IOA prospect in the Chilean iron belt. Backscattered electron imaging reveals textures of igneous and magmatic-hydrothermal affinities and the exsolution of Mn-rich ilmenite from magnetite in Quince and deep levels of Candelaria (>500 m below the bottom of the open pit). Trace element concentrations in magnetite systematically increase with depth in both deposits and decrease from core to rim within magnetite grains in shallow samples from Candelaria. These results are consistent with a cooling trend for magnetite growth from deep to shallow levels in both systems. Iron isotope compositions of magnetite range from $\delta^{56}$Fe values of 0.11 ± 0.07 to 0.16 ± 0.05‰ for Quince and between 0.16 ± 0.03 and 0.42 ± 0.04‰ for Candelaria. Oxygen isotope compositions of magnetite range from $\delta^{18}$O values of 2.65 ± 0.07 to 3.33 ± 0.07‰ for Quince and between 1.16 ± 0.07 and 7.80 ± 0.07‰ for Candelaria. For cogenetic actinolite, $\delta$D values range from –41.7 ± 2.10 to –39.0 ± 2.10‰ for Quince and from –93.9 ± 2.10 to –54.0 ± 2.10‰ for Candelaria, and $\delta^{18}$O values range between 5.89 ± 0.23 and 6.02 ± 0.23‰ for Quince and between 7.50 ± 0.23 and 7.69 ± 0.23‰ for Candelaria. The paired Fe and O isotope compositions of magnetite and the H isotope signature of actinolite fingerprint a magmatic source reservoir for ore fluids at Candelaria and Quince. Temperature estimates from O isotope thermometry and Fe# of actinolite (Fe# = [molar Fe]/([molar Fe] + [molar Mg])) are consistent with high-temperature mineralization (600°–860°C). The reintegrated composition of primary Ti-rich magnetite is consistent with igneous magnetite and supports magmatic conditions for the formation of magnetite in the Quince prospect and the deep portion of the Candelaria deposit. The trace element variations and zonation in magnetite from shallower levels of Candelaria are consistent with magnetite growth from a cooling magmatic-hydrothermal fluid. The combined chemical and textural data are consistent with a combined igneous and magmatic-hydrothermal origin for Quince and Candelaria, where the deeper portion of Candelaria corresponds to a transitional phase between the shallower IOCG deposit and a deeper IOA system analogous to the Quince IOA prospect, providing evidence for a continuum between both deposit types.

## Introduction

Iron oxide copper-gold (IOCG) and iron oxide-apatite (IOA) mineral deposits are major sources of Fe, Cu, and Au and are commonly enriched in other elements (e.g., Ag, Mo, Co, As, U, and rare earth elements [REEs]) (Hitzman et al., 1992; Hitzman, 2000; Williams et al., 2005; Groves et al., 2010; Barton, 2014; Corriveau et al., 2016). Both deposit types are structurally and/or stratigraphically controlled, are associated with extensive Na-Ca and more localized K alteration, and contain abundant Fe oxides—magnetite in IOAs and magne-

---

[†]Corresponding author: e-mail, maalromu@umich.edu

[*]Present address: Department of Geology, Universidad de Chile, Plaza Ercilla 803, Santiago, Chile.

ISSN 0361-0128; doi:10.5382/econgeo.4752; 17 p.
Digital appendices are available in the online Supplements section.

Submitted: May 24, 2019 / Accepted: January 28, 2020

tite and/or hematite in IOCGs. These deposit types are distributed globally and occur sporadically over a considerable age range from the Archean to the Pliocene (Hitzman, 2000; Williams et al., 2005; Groves et al., 2010; Barton, 2014).

Traditionally, distinct and separate genetic models have been proposed for IOCG and IOA deposits. In general, it is accepted that IOCG deposits form by hydrothermal processes where the hydrothermal ore fluid has been proposed to be a basinal brine that leaches metals from the crust (Barton and Johnson, 1996; Haynes, 2000; Benavides et al., 2007), a magmatic-hydrothermal fluid that extracts the metals from a silicate magma (Pollard, 2006), or a combination of both (Hitzman, 2000; Chiaradia et al., 2006; Groves et al., 2010; Rieger and Marschik, 2012). However, there is no consensus regarding the origin of IOA deposits. The four competing genetic models for IOA deposits are as follows: (1) a purely magmatic origin that invokes the unmixing of an intermediate silicate melt into coexisting Fe-P–rich melt and Si-rich melt where volatiles such as F, Cl, and $H_2O$ are hypothesized to preferentially partition into the Fe-P melt, making it less dense and allowing it to ascend from the source magma into the upper crust, where it crystallizes to form an IOA deposit (Nyström and Henriquez, 1994; Naslund et al., 2002; Chen et al., 2011; Tornos et al., 2017; Hou et al., 2018); (2) a magmatic-hydrothermal origin in which the fluid extracts the metals from a silicate magma (Hildebrand, 1986; Jonsson et al., 2013; Westhues et al., 2017a, b); (3) a hydrothermal metasomatic origin involving a magmatic-hydrothermal fluid (Ménard, 1995) or a mixed ore fluid that consisted of magmatic-hydrothermal and basinal brines (Rhodes and Oreskes, 1999); and (4) a combined igneous and magmatic-hydrothermal model in which primary igneous magnetite nano- and microlites serve as nucleation sites for an exsolving hypersaline magmatic-hydrothermal fluid, with hydrothermal magnetite growing from the fluid as it cools during ascent and emplacement (Knipping et al., 2015a, 2019).

In the Chilean iron belt, the spatial and temporal association of IOCG and IOA deposits has led some to suggest a genetic connection between the two deposit types, where S-Cu-Au–poor magnetite-dominated IOA deposits represent the deeper levels of S-Cu-Au–rich magnetite- and/or hematite-dominated IOCG deposits (Espinoza et al., 1996; Naslund et al., 2002; Sillitoe, 2003; Knipping et al., 2015a; Reich et al., 2016; Barra et al., 2017; Simon et al., 2018).

In this study, we investigate the geochemistry of magnetite and actinolite from drill core samples from the world-class Candelaria IOCG deposit and the Quince IOA prospect, both in the Chilean iron belt. Importantly, these two orebodies are spatially separate and did not form from the same mineralizing event. The purpose of the current study is to use the geochemistry of magnetite—the modally dominant mineral in both deposits—and actinolite to assess the hypothesis that IOCG and IOA deposit types are products of a single evolving ore system. The chemistry and textures of magnetite in samples from drill cores from both deposits were investigated using an electron probe microanalyzer (EPMA) and a scanning electron microscope (SEM) in order to evaluate the conditions and processes under which magnetite formed. Additionally, we provide the first analyses of Fe and O stable isotopes of magnetite and H stable isotopes of actinolite from these deposits to fingerprint the source of the ore fluids. Temperatures of mineralization at both deposits were estimated by using two methods: the oxygen isotope compositions of cogenetic magnetite and actinolite, and the Fe# of actinolite (Fe# = [molar Fe]/([molar Fe] + [molar Mg])).

## Geologic Background

The Chilean iron belt extends for over 800 km in the Coastal Cordillera of northern Chile and southern Peru (Fig. 1a) and contains ~50 Jurassic-Cretaceous IOA and IOCG mineral deposits hosted in Jurassic-Cretaceous volcanic sequences. In general, IOA and IOCG deposits are temporally and spatially associated and occur along curvatures and intersections of faults with different orientations (north-northeast and northwest) within the strike-slip Atacama fault system (Nyström and Henriquez, 1994; Barra et al., 2017; Veloso et al., 2017). The Atacama fault system evolved between 132 and 125 Ma from a purely extensional back-arc setting to a transtensional setting as a response to a change in the plate interactions (Brown et al., 1993; Charrier et al., 2007).

### *Quince*

Quince is an IOA prospect located ~40 km east of Chañaral, Chile (Fig. 1a). It was discovered in 1998 by an aeromagnetic survey. Geophysical data and drill core assaying were used to estimate a total resource of 2,300 million tonnes (Mt) at 30% Fe and 325.8 Mt at 0.39% $V_2O_5$. (Quince Iron Chile, 2019). The mineralization is hosted in the Late Jurassic volcanic La Negra Formation and the Cretaceous Sierra Aspera diorite and is covered by Quaternary sediments (SRK Consulting, 2014). The Quince prospect consists mainly of massive magnetite lenses and banded magnetite-calcite-quartz veins and magnetite-actinolite veins, indicating an initial mineralization event within a ductile shear zone belonging to the Atacama fault system (SRK Consulting, 2014). Stockwork-style mineralization with magnetite-rich breccias and magnetite veinlets distal to the ductile shear zone suggest a transition to a brittle regime where mineralization is mostly controlled by faulting. Magnetite is cogenetic with actinolite, which is the major accessory mineral, and apatite, diopside, calcite, quartz, and pyrite occur as modally minor phases. Sodic-calcic alteration dominated by albite and epidote is pervasive within the orebody and host rocks. Moderate potassic (K-feldspar and biotite) and quartz-chlorite-sericite alteration have also been reported in the prospect (SRK Consulting, 2014). Late-stage fractures filled with calcite and chlorite cut the main mineralization.

### *Candelaria*

The Candelaria IOCG deposit has been in production for over 20 years and is located near the city of Copiapó, Chile, in the Candelaria-Punta del Cobre district (Fig. 1). Mineral reserves as of 2018 for the Candelaria open pit and the Española project were 415 Mt at 0.48% Cu and 0.11 g/t Au (Couture et al., 2018). Mineralization consists of Fe oxides (magnetite, mushketovite, and hematite) and sulfides (pyrite, chalcopyrite, and minor pyrrhotite) and is mostly hosted in the Cretaceous volcanic to volcaniclastic Punta del Cobre Formation, which consists of the Lower Andesite, Dacite, Volcanic-sedimentary, and Upper Andesite members (del Real et al., 2018). The Punta del Cobre Formation is overlain

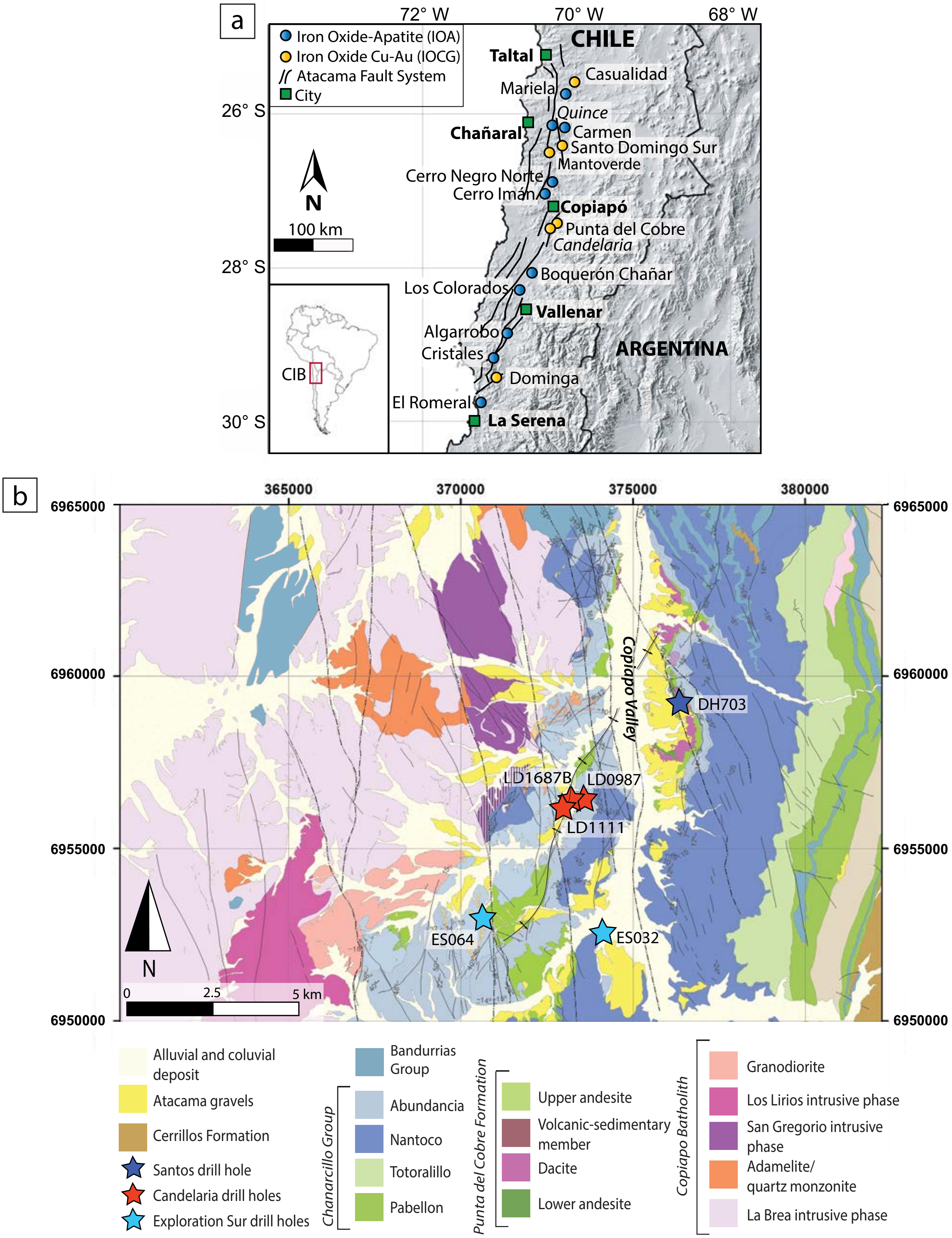

Fig. 1. a) Location of major IOA and IOCG deposits in the Chilean iron belt (CIB) along the Atacama fault system. The deposits studied are in italics. (Modified from Barra et al., 2017; Palma et al., 2019.) Inset shows location of the Chilean iron belt in South America. b) Geologic map with the location of the drill holes from the Candelaria-Punta del Cobre district. (Modified from del Real et al., 2018.)

by the marine sedimentary Chañarcillo Group, which was deposited in a shallow-marine environment associated with the development of the Chañarcillo back-arc basin (Marschik et al., 1997) and contains carbonate-bearing horizons (Marschik and Fontboté, 2001b; Mourgues, 2004; del Real et al., 2018).

Mineralization is stratigraphically and/or structurally controlled. Stratigraphically controlled bodies (commonly called "mantos") are characterized by magnetite-actinolite zones, pervasive magnetite-actinolite with potassic (biotite, K-feldspar) ± quartz alteration and disseminated sulfides (chalcopyrite, pyrrhotite ± pyrite), and overprinting biotite, magnetite (± mushketovite), chalcopyrite, pyrrhotite ± pyrite, and sphalerite veins and disseminations (del Real et al., 2018). Structurally controlled veins and breccias consist of chalcopyrite ± pyrite, actinolite, and magnetite ± mushketovite, with intense Na-Ca (albite-epidote), potassic (biotite, K-feldspar) ± quartz alteration (del Real et al., 2018).

The mineralization spanned between 118 and 112 Ma (del Real et al., 2018), with an early magnetite-actinolite event (del Real et al., 2018) overprinted by a main chalcopyrite-magnetite Cu mineralization event at 115 Ma (Marschik and Fontboté, 2001a; Mathur et al., 2002) accompanied by actinolite and potassic (biotite and K-feldspar) alteration (del Real et al., 2018). A comprehensive description of the geology, alteration, and mineralization styles of this deposit can be found in del Real et al. (2018).

Marschik and Fontboté (2001a) proposed three main stages for the formation of Candelaria based on their investigation of samples from the shallow levels of the deposit. Those authors report fluid inclusion homogenization temperatures that indicate magnetite formed between 500° and 600°C followed by sulfide-rich mineralization between 328° and 470°C and a later hematite-dominated mineralization at temperatures <300°C. The $\delta^{18}O$ values for quartz reported by Marschik et al. (2000), $\delta^{34}S$ data for anhydrite, chalcopyrite, pyrite, pyrrhotite, and sphalerite reported by Marschik and Fontboté (2001a), and in situ $\delta^{34}S$ of pyrite reported by del Real et al. (2020) support a magmatic-derived fluid as the primary ore fluid responsible for IOCG mineralization at Candelaria and mixing of the ore fluid with external (meteoric or basinal) fluid(s) during the late (low-temperature; <250°C) stage of mineralization.

## Sampling and Methods

Three core samples were collected from drill hole AQ-19 located in the southern portion of the Quince prospect. This 496-m-long drill hole traverses the magnetite veinlet-rich breccia, the massive magnetite mineralization, and the stockwork zone. Sixteen core samples from the Candelaria-Punta del Cobre district were collected from drill holes in the Santos underground mine (DH703), the Candelaria mine (LD0987, LD1111, and LD1687B), and nearby exploration targets (ES032, ES064) (Fig. 1b). Ten of the samples were collected from drill hole LD1687B, which was collared in the Candelaria open pit and was drilled to 1,147 m at an azimuth of 245° and a plunge of 60°.

### *Sample preparation*

Three samples from Quince and six samples from the Candelaria-Punta del Cobre district were mounted in epoxy resin for EPMA and SEM analyses. Eight thin sections spanning the whole length of the LD1687B Candelaria drill core were made for microscopy and EPMA studies. For isotopic analyses, magnetite was sampled from the massive magnetite horizons, or from magnetite veins where available, from the Candelaria-Punta del Cobre district and the Quince prospect. Each sample was crushed using an agate mortar and pestle, which was rinsed with ethanol and put through an ultrasonic cleaner between each sample to prevent contamination. The magnetic fraction was obtained by using a hand magnet wrapped in weighing paper, and individual, visibly unweathered magnetite grains were handpicked using a binocular microscope at ~40× magnification. Actinolite separates were obtained using a Frantz magnetic separator, followed by lithium metatungstate heavy liquid separation and handpicking of individual grains under the microscope to minimize the presence of other mineral phases. For samples where the intergrown minerals had a very small grain size, the resulting actinolite separates may have contained a small fraction of fine intergrown minerals including magnetite. Aliquots of actinolite analyzed for O isotopes, described below, were prefluorinated to remove impurities such as chlorite.

### *EPMA and field emission (FE)-SEM*

Backscattered electron (BSE) images were obtained to characterize textures by using a JEOL 7800FLV FE-SEM in the Electron Microbeam Analysis Laboratory at the University of Michigan. Point and line transect analyses were performed by using a Cameca SX-100 electron microprobe with a focused beam, a voltage of 20 keV, and a current of 30 nA for magnetite and ilmenite grains, and a 2-$\mu$m beam, 15 keV, and 20 nA for actinolite samples. Counting times, standards, and detection limits are listed in Appendix Table A1. We measured Mg, Al, Si, P, Ca, Ti, V, Cr, Mn, and Fe in magnetite and ilmenite grains, avoiding inclusions and exsolution lamellae, and executed a Ti$K\alpha$-V$K\beta$ interference correction. For actinolite grains, concentrations of Si, Ti, Al, Fe, Mn, Mg, Ca, Na, K, and P oxides were calculated from raw X-ray intensities using a ZAF intensity correction.

### *Iron isotopes*

Ion chromatography was performed on magnetite grains to isolate pure Fe from each sample. To fully dissolve each sample, approximately 2.0 mg were first digested in HF and $HNO_3$ for $\geq$24 h, dried on a hot plate, refluxed in aqua regia, and dried once more. In preparation for column chemistry, samples were dissolved in 0.5 mL 8N HCl, dried, and dissolved in 0.4 mL 8N HCl at ~120°C. The conditioning and elution procedure were completed following the procedure of Huang et al. (2011) using Biorad AG1-X8 ion exchange resin (200–400 mesh). All reactants ($HNO_3$, HCl, HF) were optima grade, and $H_2O$ was ultrapure. The stable Fe isotope analyses were performed at the Pacific Centre for Isotopic and Geochemical Research, University of British Columbia, using a Nu Plasma 1700 multicollector-inductively coupled plasma-mass spectrometer (MC-ICP-MS) in dry plasma mode with a DSN-100 desolvating nebulizer system. All analyses were performed in true high-resolution mode as isobaric interferences (i.e., Ar complexes) were fully resolved from the Fe isotopes ($^{54}Fe$, $^{56}Fe$, $^{57}Fe$). Minor Cr corrections were done online for each analysis by monitoring $^{52}$Cr. Every sample was measured between two and four times and was bracketed immediately before and after analysis by the measurement of standard 14 from the Institute for Reference Materials and Measurements (IRMM-14). The concentration of the samples was adjusted to be within 10% of the bracketing standard solution.

### *Oxygen and hydrogen isotopes*

The isotopic ratio of $\delta^{18}$O standard mean ocean water (SMOW) of magnetite and actinolite separates (1.5–2.1 mg each) was measured at the University of Oregon using $BrF_5$ in a laser fluorination line connected to a Thermo-Finnigan MAT 253 gas isotope ratio mass spectrometer (IRMS) in dual inlet mode. The Gore Mountain garnet (GMG) standard (6.52‰) and UWG-2 garnet (5.8‰) were measured prior, during, and after the sample analyses to quantify them onto an SMOW scale (Loewen and Bindeman, 2016). Yields ($\mu$mol/mg of extracted $O_2$ gas) were monitored by a Barathron gauge. The water content and stable $\delta$D isotopic ratios of actinolite samples were measured by thermal pyrolysis using thermal conversion elemental analyzer attached to a MAT 253 IRMS by a continuous flow method, also at the University of Oregon. We used a glassy carbon reactor held at 1,450°C following the analytical procedures described in Bindeman et al. (2012). For standards we used new USGS57 and 58 micas (Qi et al., 2017), and our analyses had a precision of ±0.03 wt % water and ±2‰ $\delta$D.

### *Reintegration of ilmenite exsolution lamellae and granules in magnetite*

We selected six BSE images from three samples from Quince and seven BSE images from three Candelaria samples that contain magnetite and ilmenite. We used the difference in grayscale between magnetite and ilmenite to do a supervised image classification and estimate the fraction of magnetite and ilmenite in each image by using the Python programming language. We then normalized the mineral fractions with their respective average Ti, V, Al, and Mn concentrations to a single magnetite phase.

## Results

### *Core sample descriptions*

*Candelaria:* The upper part of drill core LD1687B intersects layered sedimentary rocks replaced by magnetite, traverses the manto massive magnetite (± mushketovite) mineralization, and then cuts through magnetite- and actinolite-rich horizons at greater depth (Fig. 2a-f). Pyrite, chalcopyrite, and minor pyrrhotite are present disseminated or in veins and decrease in abundance with depth. Sodic-calcic (actinolite, albite, epidote) and potassic (K-feldspar ± biotite) are the dominant alteration assemblages. Late-stage quartz and anhydrite veins crosscut primary mineralization, and secondary chlorite is also present (Fig. 2f). Other accessory minerals in the Candelaria-Punta del Cobre district only identified in thin section include apatite, calcite, ilmenite, and titanite. Detailed hand sample descriptions are provided in Table 1.

*Quince*: Representative scans of drill core samples of the magnetite veinlet-rich breccia, massive magnetite, and magnetite from the stockwork zone are shown in Figure 2g, h, and i, respectively. Magnetite (modal abundance of ~95%) and actinolite (modal abundance of ~5%) are intergrown with each other and occur in the groundmass and as veinlets (Fig. 2i). Apatite and diopside are minor accessory phases. Disseminated pyrite is present but is modally insignificant. The main alteration in the deposit is sodic-calcic (albite ± scapolite ± epidote). Late-stage quartz (± chlorite) veins crosscut the main mineralization. Detailed hand sample descriptions are provided in Table 1.

### *Magnetite textures and associated minerals*

The BSE images of magnetite from the Candelaria-Punta del Cobre district reveal two magnetite textures (Table 2). Type C is characterized by euhedral magnetite lacking visible exsolution lamellae and few or no visible aluminosilicate or other inclusions (Fig. 3a, e). Type D refers to both mushketovite (hematite that has been replaced by magnetite) that exhibits patchy zonation and magnetite that exhibits concentric (core and rim) zonation between relatively dark and light areas, where the dark areas are locally inclusion rich (Fig. 3b, c). Magnetite type C is present throughout the entire LD1687B hole. Magnetite type D was only identified in shallower samples (i.e., <500 m deep). Magnetite grains with ilmenite exsolution lamellae—type B at Quince as described below—were not observed in any Candelaria samples. Magnetite grains from the deep samples (>500 m below the bottom of the open pit) in the Candelaria drill hole LD1687B, however, are intimately related with ilmenite that occurs as fracture infill (Fig. 3d) or as granules adjacent to magnetite grains (Fig. 3f).

The BSE images from Quince reveal three magnetite textures (Table 2): magnetite rich in Fe-Mg silicate and aluminosilicate inclusions (type A), magnetite that contains abundant ilmenite exsolution lamellae forming trellis and cloth textures (type B), and euhedral magnetite without visible inclusions or exsolution lamellae (type C) (Fig. 3g-i). All three textures are observed throughout the entire length of the sampled drill hole, and there is no textural zonation observed within grains. In magnetite type B, trellis texture is predominant in the deepest sample (404 m), while cloth-textured exsolution lamellae are visibly more abundant than trellis-textured lamellae in the shallowest sample (68 m). The sample from intermediate depth (334 m) shows both textures in similar proportions. Magnetite grains of all textural types commonly meet at triple junctions (Fig. 3g-i). Ilmenite and, to a lesser extent, rutile are present along grain boundaries and fill interstices among magnetite (mostly type C) grains. Interstitial ilmenite and rutile are more abundant in shallower samples, and their occurrence is inversely proportional to the quantity of exsolution lamellae in magnetite (Fig. 3g).

### *Trace element compositions of magnetite*

All EPMA data for magnetite and ilmenite are provided in Appendix Table A2. Summary statistics for magnetite and ilmenite as a function of sample depth are provided in Appendix Tables A3 through A6.

Magnetite from Quince averages 71.8 ± 0.8 wt % Fe. Iron, Si, and Cr in magnetite generally increase with depth throughout the drill hole, while Al, Ti, and Mn generally decrease. Vanadium and Ca show no significant variation with depth,

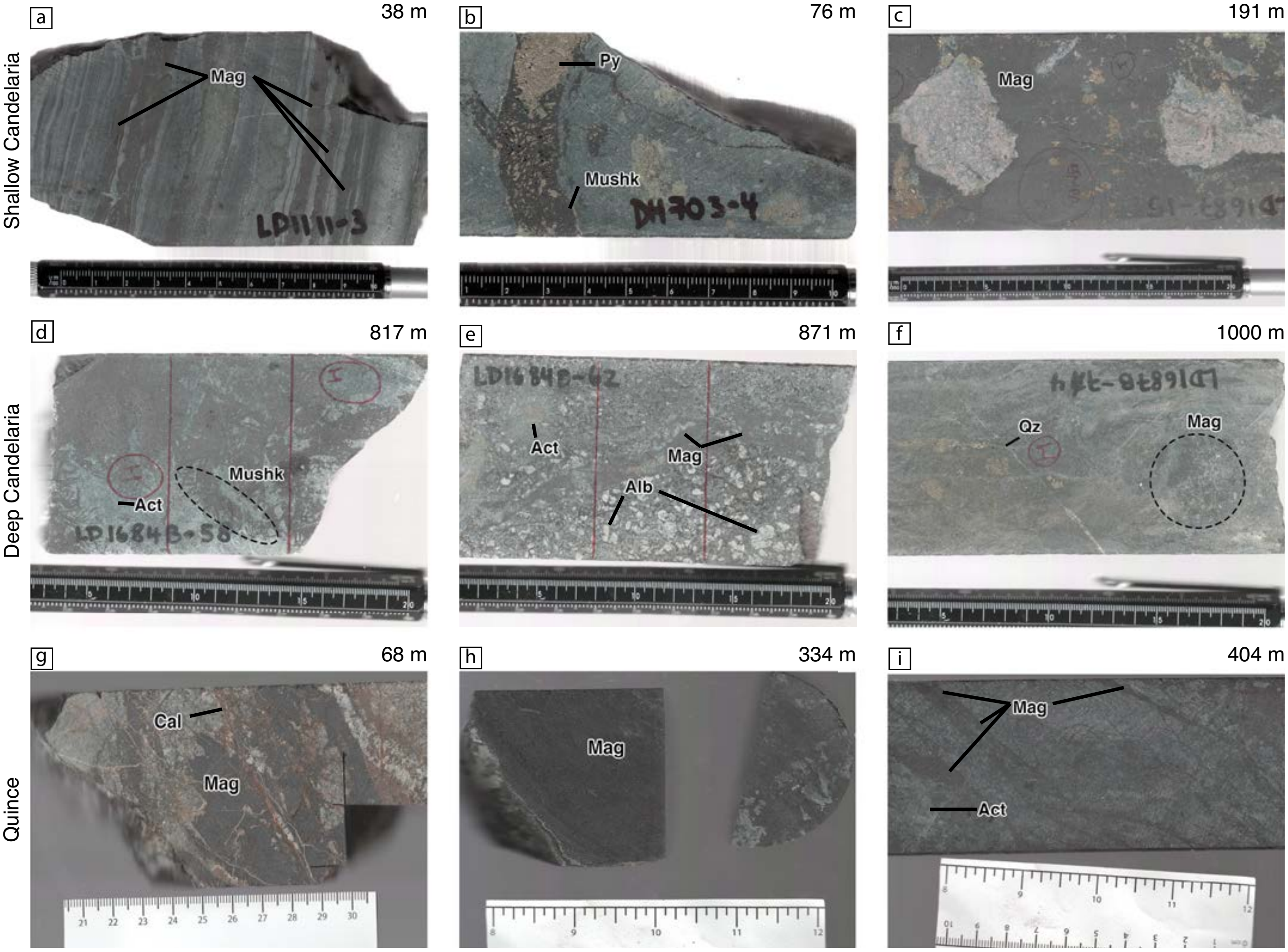

Fig. 2. Representative drill core samples divided as follows: shallow Candelaria, deep Candelaria, and Quince. Sample depths are indicated in the top right corner of each picture and increase from left to right. Detailed sample descriptions are in Table 1. a) Sample LD1111 3 showing intercalation of magnetite-rich and magnetite-poor bands. b) Sample DH703 4 showing mushketovite plus sulfide vein. c) Sample LD1687B 15 with magnetite matrix, disseminated pyrite and chalcopyrite, and altered andesitic clasts. d) Sample LD1687B 58 showing intergrown actinolite and mushketovite. e) Sample LD1687B 62 showing albitization, fine-grained actinolite and magnetite in the matrix, and magnetite veins with less pyrite and chalcopyrite compared to the veins at shallower levels. f) Sample LD1687B 74 with disseminated magnetite and minor pyrite and chalcopyrite. A late-stage quartz veinlet cuts the main mineralization. g) Sample AQ-19 4 showing brecciated magnetite vein with later calcite-siderite veinlets. h) Massive magnetite from sample AQ-19 3. i) Sample AQ-19 2 with magnetite intergrown with actinolite in matrix. Act = actinolite, Alb = albitization, Cal = calcite/siderite, Mag = magnetite, Mushk = mushketovite, Py = pyrite, Qz = quartz.

and Mg fluctuates nonsystematically. Interstitial ilmenite is enriched in Mn, containing an average Mn concentration of 5.1 ± 2.4 wt %.

Magnetite from the Candelaria-Punta del Cobre district contains 71.3 ± 1.06 wt % Fe. The concentrations of Mg, Al, Ca, V, and Cr in magnetite generally increase with depth, whereas Mn generally decreases. Iron, Si, and Ti concentrations in magnetite do not show systematic variations with depth, but the concentration of Ti in magnetite is higher in samples where ilmenite is present. The rims of zoned magnetite grains (type D) from shallow samples are enriched in Fe (71.8 wt % Fe) and depleted in trace elements (0.01 wt % Cr, 0.04 wt % Ca, 0.05 wt % Al, 0.05 wt % Mn, 0.08 wt % Ti, 0.09 wt % Mg, 0.19 wt % Si) relative to cores (70.1 wt % Fe, 0.03 wt % Cr, 0.16 wt % Ca, 0.12 wt % Al, 0.07 wt % Mn, 0.11 wt % Ti, 0.22 wt % Mg, 0.73 wt % Si). Ilmenite granules are Mn rich (avg 4.3 ± 2.6 wt % Mn; maximum 10.9 wt % Mn).

### *Ilmenite reintegration in magnetite*

The EPMA Ti, V, Mn, and Al contents of individual ilmenite and magnetite grains from the analyzed BSE images and the results for the mineral fraction estimations and the reintegration of ilmenite into host magnetite are summarized in Appendix Table A7. After the reintegration, the calculated concentrations of Ti, V, Al, and Mn (wt %) vary between 0.53 and 2.92, 0.00 and 0.03, 0.00 and 0.03, and 0.05 and 0.35, respectively, for the samples from Candelaria and between

Table 1. Sample Descriptions

| Area | Drill core | Sample | Vertical depth from collar (m) | Elevation from sea level (m) | Macroscopic highlights |
|---|---|---|---|---|---|
| Quince | AQ-19 | 4 | 68 | 631 | Brecciated magnetite veins in sodic-calcic altered groundmass with calcite-siderite veins |
| Quince | AQ-19 | 3 | 334 | 362 | Massive magnetite with disseminated sulfides and chlorite product of alteration |
| Quince | AQ-19 | 2 | 404 | 294 | Sodic-calcic–altered groundmass with magnetite-actinolite ductile bands; late, chlorite-calcite veins crosscut |
| Santos | DH703 | 4 | 76 | 549 | Altered andesitic rock with potassic alteration (biotite and K-feldspar) and a mushketovite vein that contains massive pyrite |
| Candelaria | LD1111 | 3 | 38 | 394 | Volcano-sedimentary unit with bands that have been replaced by magnetite and subsequently microfaulted; pervasive sodic-calcic alteration in the rest of the layers was affected by subsequent silicification |
| Candelaria | LD1111 | 18 | 398 | 34 | Magnetite-actinolite breccia with veins of massive pyrite and calcite accompanied by secondary epidote |
| Candelaria | LD0987 | 9 | 493 | 29 | Andesitic rock with potassic alteration (K-feldspar) and chlorite; veins of pyrite and chalcopyrite; minor, fine, disseminated magnetite |
| Exploration Sur | ES032 | 12 | 743 | –35 | Sample from the manto mineralization; massive magnetite aggregates and actinolite; abundant disseminated pyrite; potassic alteration and scattered secondary epidote |
| Exploration Sur | ES064 | 19 | 1,091 | –299 | Pervasively albitized groundmass with patches and veinlets of magnetite; posterior K-feldspar veins contain massive, euhedral pyrite |
| Candelaria | LD1687B | 6 | 80 | 395 | Volcano-sedimentary unit with bands that have been replaced by magnetite; subsequent chloritization and silicification |
| Candelaria | LD1687B | 12 | 133 | 342 | Undifferentiated matrix with magnetite fragments; sulfides present in their borders and fractures |
| Candelaria | LD1687B | 15 | 191 | 284 | Disseminated sulfides (py, cpy) and massive magnetite in breccia with potassic-altered andesitic clasts |
| Candelaria | LD1687B | 34 | 486 | –11 | Abundant sulfides (py, cpy, po) in magnetite breccia with clasts pervasively altered to chlorite |
| Candelaria | LD1687B | 43 | 618 | –143 | Breccia with sodic-calcic–altered groundmass with few disseminated sulfides and massive magnetite clasts |
| Candelaria | LD1687B | 52 | 731 | –256 | Mushketovite and potassic feldspar veins in fine, undifferentiated matrix |
| Candelaria | LD1687B | 58 | 817 | –342 | Massive mushketovite and minor actinolite in altered volcanic matrix |
| Candelaria | LD1687B | 61 | 840 | –365 | Albitized volcanic rock with a massive magnetite vein crosscut by a chlorite vein; posterior K-feldspar veins contain sulfides |
| Candelaria | LD1687B | 62 | 871 | –396 | Porphyritic rock with K-feldspar veins cutting magnetite veins |
| Candelaria | LD1687B | 74 | 1,000 | –525 | Disseminated magnetite in volcanic rock; minor sulfides and late-stage quartz veins |

Abbreviations: cpy = chalcopyrite, po = pyrrhotite, py = pyrite

0.56 and 3.03, 0.15 and 0.17, 0.03 and 0.05, and 0.10 and 0.70 for the Quince samples.

### Actinolite chemistry

All EPMA data for actinolite are provided in Appendix Table A2. Average compositions for three Candelaria samples at progressively greater depth downhole—43 (617.8 m), 52 (731.3 m), and 58 (846.5 m) in drill hole LD1687B—and Quince sample 2 (downhole depth = 404.3 m) are summarized in Table 3. On average, the actinolite from Candelaria is enriched in FeO (11.3–13.2 wt %) and CaO (12.2 wt %) and depleted in $TiO_2$ (0.12–0.27 wt %), $Al_2O_3$ (3.21–4.14 wt %), MgO (15.5–16.5 wt %), and $Na_2O$ (0.36–0.50 wt %) with respect to the actinolite from Quince (8.94 FeO, 11.6 CaO, 0.38 $TiO_2$, 4.35 $Al_2O_3$, 18.9 MgO, and 0.73 $Na_2O$ wt %). The average Ca (atoms per formula unit [apfu]) content of actinolite in the Candelaria samples was 2.03, and it was 1.90 for the Quince sample (Table 3). For the same samples, the Fe number of actinolite (Fe# = [molar Fe]/([molar Fe] + [molar Mg])) was calculated by following the methodology by Lledo and Jenkins (2008). The actinolite grains yielded an average Fe number $\pm 2\sigma$ of 0.29 ± 0.11, 0.28 ± 0.05, 0.32 ± 0.05, and 0.21 ± 0.05, respectively.

Table 2. Magnetite Types

| Type | Occurrence | Inclusion | Zoning | Other features |
|---|---|---|---|---|
| A | Quince | Rich | Absent | |
| B | Quince | Poor | Absent | Ilmenite exsolution lamellae |
| C | Quince and Candelaria | Absent | Absent | Associated to ilmenite (interstitial or as granules) |
| D | Shallow Candelaria | Localized | Concentric or patchy | |

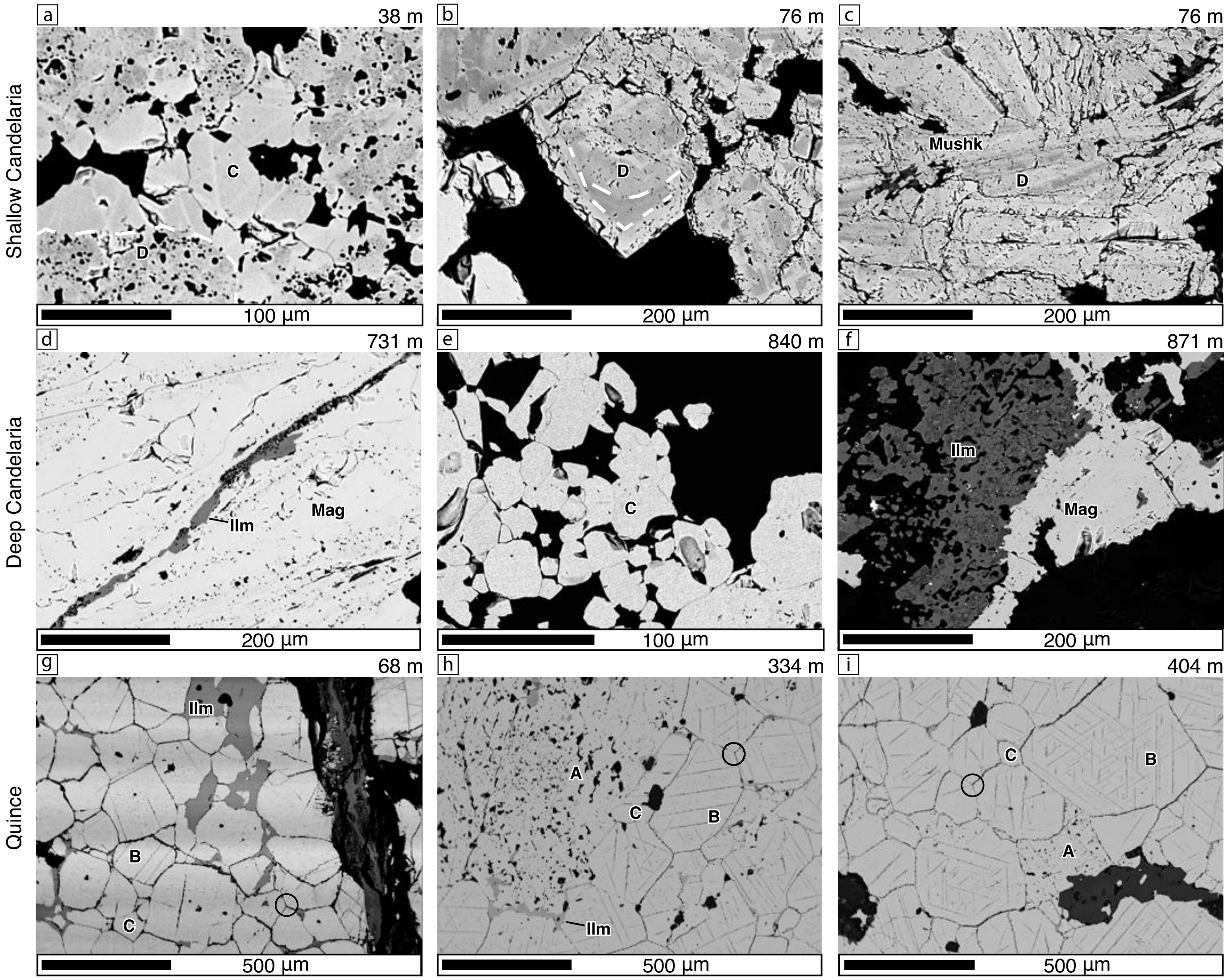

Fig. 3. Backscattered electron images from selected samples. Organization as in Figure 2. a) Sample LD1111 3 showing magnetite type C (center) and D (lower left), where the dashed line shows the boundary between the dark, inclusion-rich core and the lighter, inclusion-free rim. b) Sample DH7034 showing magnetite type D with core-rim zonation and sulfides (bright grains in lower left corner). The dashed lines separate the darker core from the lighter rim. c) Sample DH 703 4 showing mushketovite grains with darker and light areas (magnetite type D with patchy zonation). d) Sample LD1687B 52 showing ilmenite and rutile filling fractures between magnetite grains. e) Sample LD1687 61 showing magnetite type C. f) Sample LD1687 62 where magnetite is intimately related to ilmenite granules. Note the absence of exsolution textures in magnetite. g) Sample AQ-19 4 with triple junctions (in circle), interstitial ilmenite, and magnetite types C and B with predominantly cloth texture and lesser trellis texture. h) Sample AQ-19 3 showing triple junctions and magnetite types A, C, and B with trellis and cloth textures. Ilmenite filling interstices but in less proportion relative to the shallower sample AQ-19 4. i) Sample AQ-19 2 with magnetite types A, C, and B with abundant exsolution lamellae forming trellis textures and minor cloth texture. Interstitial ilmenite is less abundant than at shallower levels. Abbreviations: Ilm = ilmenite, Mag = magnetite, Mushk = mushketovite.

Table 3. Actinolite Chemistry (average per sample; in wt %)

| Drill core | Sample | Points per sample | $SiO_2$ | $TiO_2$ | $Al_2O_3$ | FeO | MnO | MgO | CaO | $Na_2O$ | $K_2O$ | Total | Ca (apfu) | Fe# | Estimated temperature (°C ± 2σ) 100 MPa | 400 MPa |
|---|---|---|---|---|---|---|---|---|---|---|---|---|---|---|---|---|
| LD1687B | 43 | 23 | 51.2 | 0.14 | 4.14 | 12.1 | 0.22 | 16.2 | 12.2 | 0.36 | 0.15 | 96.7 | 2.03 | 0.29 | 752 ± 36 | |
| LD1687B | 52 | 10 | 51.9 | 0.27 | 3.21 | 11.3 | 0.23 | 16.5 | 12.2 | 0.50 | 0.18 | 96.3 | 2.03 | 0.28 | 756 ± 18 | |
| LD1687B | 58 | 5 | 51.4 | 0.12 | 3.74 | 13.2 | 0.25 | 15.5 | 12.2 | 0.43 | 0.24 | 97.0 | 2.03 | 0.32 | 741 ± 18 | |
| AQ-19 | 2 | 9 | 51.8 | 0.38 | 4.35 | 8.94 | 0.24 | 18.9 | 11.6 | 0.73 | 0.20 | 97.0 | 1.90 | 0.21 | 782 ± 18 | 830 ± 18 |

### *Iron isotope compositions of magnetite separates*

Table 4 summarizes the Fe isotope data for the 16 magnetite samples relative to the IRMM-14. Analyses of the reference material BCR-2 yielded an average value of 0.09 ± 0.03‰ ($n$ = 12), which is consistent with the value of 0.09 ± 0.01‰ ($n$ = 8) recommended by Craddock and Dauphas (2011). The $\delta^{56}$Fe ±2$\sigma$ values for magnetite from Quince range between 0.11 ± 0.07 and 0.16 ± 0.05‰ and yield an average value of 0.13 ± 0.03‰ ($n$ = 3). The samples from Candelaria range between 0.16 ± 0.03 and 0.42 ± 0.04‰ and yield an average of 0.23 ± 0.04‰ ($n$ = 13).

### *Oxygen and hydrogen isotope compositions of magnetite and actinolite separates*

Oxygen isotope data for 15 magnetite and five actinolite samples (Table 4) are reported relative to the international Vienna-standard mean ocean water (V-SMOW) standard. Analyses of the standard GMG yielded $\delta^{18}$O ±2$\sigma$ values of 6.24 ± 0.07 and 6.42 ± 0.23‰ over two days of measurements for the magnetite samples, and 6.48 ± 0.23‰ for the actinolite samples. The analytical values were corrected by using the difference between the measured and the expected value for the standard for each day.

The $\delta^{18}$O ±2$\sigma$ values for magnetite from Quince range between 2.65 ± 0.07 and 3.33 ± 0.07‰ and have an average $\delta^{18}$O ±2$\sigma$ value of 3.04 ± 0.4‰ ($n$ = 3). The samples from Candelaria yielded $\delta^{18}$O ±2$\sigma$ values that range from 1.16 ± 0.07 to 7.80 ± 0.07‰ and have an average $\delta^{18}$O ±2$\sigma$ value of 3.52 ± 0.94‰ ($n$ = 12). The average $\delta^{18}$O ±2$\sigma$ values for actinolite are 5.96 ± 0.13 ($n$ = 2) and 7.57 ± 0.12‰ ($n$ = 3) for Quince and Candelaria, respectively.

Hydrogen isotope values of actinolite samples relative to V-SMOW are compiled in Table 4. The $\delta$D ±2$\sigma$ values for actinolite from Quince average –40.4 ± 2.7‰ ($n$ = 2), and from Candelaria average –67.3 ± 18.0‰ ($n$ = 4), with the lightest value corresponding to the shallowest sample. The water content (wt % $H_2O$ ±2$\sigma$) of actinolite from Quince averages 2.00 ± 0.03 wt % ($n$ = 2), and actinolite from Candelaria averages 1.97 ± 0.89 wt % ($n$ = 4). The low $H_2O$ concentration and the light $\delta$D value measured for sample 6 from the LD1687B drill hole may reflect the presence of some chlorite and magnetite identified in hand sample (Table 1).

## Discussion

### *Constraints on magnetite and actinolite formation*

The inclusion-rich magnetite (type A) from Quince (Fig. 3h, i) is similar to magnetite reported in drill core from the El Laco (Ovalle et al., 2018), Los Colorados (Knipping et al., 2015b), and El Romeral (Rojas et al., 2018) IOA deposits in Chile. Those authors concluded that El Laco, Los Colorados, and El Romeral formed by a combination of igneous and magmatic-hydrothermal processes, based on the stability of the magnetite-hosted mineral inclusions (all three deposits) and the presence of ilmenite exsolution lamellae (El Laco and El Romeral) in magnetite. Magnetite grains with trellis- and cloth-textured ilmenite exsolution lamellae, as observed in type B magnetite in Quince, are common in igneous rocks and Fe-Ti oxide deposits hosted in mafic intrusions (Buddington and Lindsley, 1964; Carmichael, 1966; Haggerty, 1976; Pang et al., 2008; Tan et al., 2016; Arguin et al., 2018) but to our knowledge have only been reported in a few studies of IOA

Table 4. Isotopic Results

| | | Magnetite | | | | | | | | Actinolite | | | | | | Estimated temperature |
|---|---|---|---|---|---|---|---|---|---|---|---|---|---|---|---|---|
| Drill core | Sample | $\delta^{56}$Fe (‰) | 2sd | n56 | $\delta^{57}$Fe (‰) | 2sd | n57 | $\delta^{18}$O (‰) | 2sd | $\delta$D (‰) | 2sd | $H_2O$ (wt %) | 2sd | $\delta^{18}$O (‰) | 2sd | (°C ± 2sd) |
| AQ-19 | 4 | 0.16 | 0.05 | 4 | 0.26 | 0.08 | 3 | 3.33 | 0.07 | | | | | | | |
| AQ-19 | 3 | 0.11 | 0.07 | 3 | 0.27 | 0.05 | 3 | 2.65 | 0.07 | | | | | | | |
| AQ-19 | 2 | 0.13 | 0.04 | 4 | 0.18 | 0.14 | 4 | 3.13 | 0.07 | –39.0 | 2.10 | 2.01 | 0.08 | 5.89 | 0.23 | 835 ± 20 |
| AQ-19 | 2 | | | | | | | | | **–41.7** | 2.10 | **1.98** | 0.08 | **6.02** | 0.23 | 860 ± 20 |
| DH703 | 4 | 0.21 | 0.06 | 3 | 0.33 | 0.06 | 2 | 1.16 | 0.07 | | | | | | | |
| LD1111 | 3 | 0.16 | 0.06 | 3 | 0.22 | 0.08 | 3 | 7.80 | 0.07 | | | | | | | |
| LD1111 | 18 | 0.20 | 0.04 | 3 | 0.18 | 0.05 | 3 | 3.55 | 0.07 | | | | | | | |
| ES064 | 19 | 0.23 | 0.05 | 3 | 0.35 | 0.15 | 3 | | | | | | | | | |
| LD1687B | 6 | 0.20 | 0.03 | 4 | 0.28 | 0.06 | 4 | 5.03 | 0.23 | –93.9 | 2.10 | 0.81 | 0.08 | | | |
| LD1687B | 12 | 0.17 | 0.06 | 3 | 0.32 | 0.24 | 3 | 3.65 | 0.23 | | | | | | | |
| LD1687B | 15 | 0.21 | 0.04 | 3 | 0.33 | 0.09 | 3 | 2.59 | 0.23 | | | | | | | |
| LD1687B | 34 | 0.42 | 0.04 | 3 | 0.65 | 0.25 | 3 | 2.50 | 0.23 | | | | | | | |
| LD1687B | 43 | 0.26 | 0.10 | 4 | 0.40 | 0.23 | 4 | 2.95 | 0.23 | –57.4 | 2.10 | 2.84 | 0.08 | *7.69* | 0.23 | 591 ± 20 |
| LD1687B | 58 | 0.21 | 0.06 | 4 | 0.25 | 0.05 | 4 | 3.21 | 0.23 | | | | | | | |
| LD1687B | 61 | 0.16 | 0.03 | 3 | 0.30 | 0.21 | 3 | 3.50 | 0.23 | –64.0 | 2.10 | 1.75 | 0.08 | *7.53* | 0.23 | 665 ± 20 |
| LD1687B | 62 | 0.30 | 0.07 | 3 | 0.45 | 0.13 | 3 | 3.50 | 0.23 | | | | | | | |
| LD1687B | 74 | 0.26 | 0.02 | 3 | 0.39 | 0.09 | 3 | 2.81 | 0.07 | –54.0 | 2.10 | 2.47 | 0.08 | *7.50* | 0.23 | 595 ± 20 |
| Averages | | | | | | | | | | | | | | | | |
| Candelaria | | 0.23 | 0.04 | | 0.34 | 0.07 | | 3.52 | 0.94 | –67.3 | 18.20 | 1.97 | 0.89 | 7.57 | 0.12 | |
| Quince | | 0.13 | 0.03 | | 0.24 | 0.06 | | 3.04 | 0.40 | –40.4 | 2.70 | 2.00 | 0.03 | 5.96 | 0.13 | |

Notes: bold numbers indicate single crystal, italics indicate prefluorinated, blank cells indicate no data; n56 and n57 refer to the number of measurements per sample of the $^{56}$Fe and $^{57}$Fe isotopes

Abbreviation: sd = standard deviation

deposits (e.g., Malmberget: Lund, 2013; El Laco: Ovalle et al., 2018; El Romeral: Rojas et al., 2018; Gushan: Sun et al., 2019) and in the Sossego IOCG deposit (Huang and Beaudoin, 2019). The presence of trellis- and cloth-textured exsolution lamellae results from oxyexsolution of primary Ti-rich magnetite. The process of oxyexsolution was first described by Buddington and Lindsley (1964), who experimentally demonstrated that at 550° to 1,000°C in the $FeO\text{-}Fe_2O_3\text{-}TiO_2$ system, a solid solution exists between magnetite and ulvöspinel ($Fe_2TiO_4$). If magnetite-ulvöspinel$_{SS}$ cools in a water-rich system, the ulvöspinel component of the solid solution is directly oxidized to magnetite and ilmenite, where the latter exsolves along the (111) planes of magnetite (Buddington and Lindsley, 1964; Haggerty, 1976). Trellis and cloth textures can coexist in a single magnetite grain, but cloth texture is generated at lower temperatures than trellis texture (Neybergh et al., 1980; Gruenewaldt et al., 1985). In Quince, the transition from trellis-dominated to cloth-dominated textures in magnetite grains from deep to shallow levels indicates cooling of the system and correlates with increasing proportions of interstitial ilmenite and inclusion-free magnetite (type C) at shallower levels (Fig. 3g-i). The presence of ilmenite exsolution lamellae in magnetite grains and coating grain boundaries in samples from Quince is evidence for primary Ti-rich magnetite growth at magmatic or near-magmatic temperatures.

The $Al_2O_3$ and $TiO_2$ compositions of actinolite are directly proportional to the temperature and pressure conditions at which they formed (Mark and Foster, 2000, and references therein). The elevated content of these oxides in actinolite from the deeper samples at Candelaria and Quince are consistent with mineralization at high-temperature conditions (Table 3; App. Table A2).

The temperature of mineralization for Quince was estimated using the Fe# of actinolite, which is coeval with magnetite, following Lledo and Jenkins (2008). Those authors experimentally demonstrated the upper stability of natural actinolite from the Pleito Melón IOA deposit in Chile (Fe# = 0.22 and Ca apfu = 1.97) to be ~780°C at 100 MPa and 850°C at 400 MPa. The Ca apfu of actinolite from Quince is similar to that reported by Lledo and Jenkins (2008), which allows us to use their model to estimate the temperature of actinolite crystallization. The Fe# of actinolite of the Quince samples yields a formation temperature of 795°C at 100 MPa and 830°C at 400 MPa (Table 3). These temperatures are within the range of 610° to 820°C estimated by Bilenker et al. (2016) for actinolite from the Los Colorados IOA deposit, Chile, and 735° to 840°C estimated by Rojas et al. (2018) for actinolite from the El Romeral IOA deposit, Chile, by using the Fe# method. The textural association of actinolite and magnetite in samples from Quince is similar to that reported for Los Colorados (Bilenker et al., 2016), El Romeral (Rojas et al., 2018), and Cerro Negro Norte (Salazar et al., 2020). The composition of actinolite from Quince is also similar to that reported from actinolite from the aforementioned studies and indicates mineral growth at magmatic to magmatic-hydrothermal conditions, which is consistent with the conclusions reported for mineralization at Los Colorados, El Romeral, and Cerro Negro Norte. We note that the $\delta D$ values of actinolite cogenetic with magnetite in Quince and the deeper samples from Candelaria (Table 4) are consistent with a high-temperature, magmatic source when paired with their O isotope values (Taylor, 1974; Hedenquist and Lowenstern, 1994), as has been reported for actinolite from the Los Colorados IOA deposit (Bilenker et al., 2016).

We also estimated the temperature of mineralization at Quince by using the oxygen isotope fractionation factor between actinolite and magnetite using the equation

$$\delta^{18}\,O_{\text{actinolite}}\text{-}\delta^{18}\,O_{\text{magnetite}}=\Delta^{18}\,O_{\text{actinolite-magnetite}}$$

$$\sim 1000\, ln\, \alpha = 10^6 \times \frac{A}{T^{2'}}, \tag{1}$$

where $\Delta^{18}O_{\text{actinolite-magnetite}}$ was calculated using the measured isotopic compositions of sample AQ-19 2. An A factor of 3.54 for diopside (a close analogue to actinolite; Chiba et al., 1989) was used as a proxy for actinolite, as no direct experimental data for actinolite are available. We highlight that the analyzed magnetite grains contain ilmenite exsolution lamellae and that the bulk magnetite-ilmenite oxygen isotope ratios are likely representative of the primary Ti-rich magnetite and not affected by exsolution, as magnetite is the dominant phase and is buffered (cf. Valley, 2001). The magnetite-actinolite pairs from the deepest level of Quince yield calculated temperatures of 835° and 860°C. These model temperatures for magnetite are consistent with the high temperatures estimated from actinolite chemistry and indicate formation of primary igneous magnetite-ulvöspinel$_{SS}$ that unmixed during cooling and subsequent oxidation to magnetite and ilmenite, where the latter is present as exsolution lamellae in magnetite and interstitially coating grain boundaries among magnetite grains (Fig. 3g-i). The agreement between temperatures of mineralization estimated by using the Fe# of actinolite and $\Delta^{18}O_{\text{actinolite-magnetite}}$ suggests that the two phases crystallized in equilibrium with one another (cf. Farquhar et al., 1993; Valley, 2001).

We did not observe ilmenite exsolution lamellae in any magnetite grains from Candelaria as described above for magnetite type B in Quince. However, the presence of ilmenite granules intimately associated with magnetite in the deepest Candelaria samples (e.g., Fig. 3f; >800 m below the bottom of the open pit) and the interstitial ilmenite in Quince samples are consistent with the granule oxyexsolution process described by Buddington and Lindsley (1964). Those authors report that granular ilmenite is produced by fluid-mediated oxyexsolution of primary magnetite-ulvöspinel$_{SS}$ that results in complete exsolution of ilmenite from magnetite. Granular oxyexsolution occurs by subsolidus oxidation of magnetite-ulvöspinel$_{SS}$ by reaction with intergranular fluid. The presence of triple junctions among magnetite grains in both deposits (Fig. 3e, g-i) and of interstitial ilmenite in the Quince samples (Fig. 3g, h) are evidence for reequilibration of primary Ti-rich magnetite and reprecipitation of pristine, hydrothermal magnetite (type C) and interstitial ilmenite in the presence of a high-temperature fluid (Hu et al., 2014; Heidarian et al., 2016; Ovalle et al., 2018). The decrease in ilmenite exsolution lamellae in magnetite, coupled with the increase in interstitial ilmenite from deep to shallow levels in Quince, and the ilmenite granules in deeper samples from Candelaria are consistent with migration of exsolved ilmenite outside of the magnetite crystal structure by reaction with high-temperature hydrothermal fluid—potentially during the ore-forming mineralization process. The presence of interstitial rutile with ilmenite and magnetite is also evidence for reequilibration of original Ti-rich magnetite under hydrothermal conditions at temperatures ranging from 400° to 700°C as reported in studies of porphyry copper deposits (Rabbia et al., 2009; Rabbia and Hernández, 2012).

The temperatures of crystallization for actinolite in Candelaria samples LD1987B 43, 52, and 58 estimated following Lledo and Jenkins (2008) at 100 MPa are 752°, 756°, and 741°C, respectively (Table 3). The actinolite-magnetite pair ($\Delta^{18}O_{\text{actinolite-magnetite}}$) approach yielded minimum temperatures of formation of 591°, 665°, and 595°C for samples LD1987B 43, 61, and 74 (Table 4). The lack of agreement for temperatures at Candelaria estimated using the Fe# of actinolite and $\Delta^{18}O_{\text{actinolite-magnetite}}$ pairs likely reflects uncertainties in the thermodynamic model of Lledo and Jenkins (2008) used to calculate model temperatures from the Fe# of actinolite and possibly O isotope resetting of magnetite and/or actinolite during cooling. The actinolite composition for the Candelaria samples LD1987B 43, 52, and 58 yields an average Ca apfu of 2.03, which is slightly higher than the Ca apfu value of 1.8 that Lledo and Jenkins (2008) used to derive the thermodynamic model from their experimental data. According to Lledo and Jenkins (2008), increasing the Ca apfu by 0.3 overestimated the temperature of actinolite crystallization in their experiments by 25°C. Thus, the model temperatures calculated from the Fe# of Candelaria actinolite may similarly be overestimated when considering the Ca content of actinolite. If mineralization at Candelaria occurred at a pressure <100 MPa, and if we assume a linear relationship for Fe# and temperature from 100 to 400 MPa as experimentally determined by Lledo and Jenkins (2008), extrapolating to pressures <100 MPa would also result in overestimation of Fe# temperatures by approximately 20°C/100 MPa.

For the temperatures estimated by using the $\Delta^{18}O_{\text{actinolite-magnetite}}$ method, Edwards and Valley (1998) reported that variable $f_{(H_2O)}$ during cooling promotes faster diffusion and resetting of $\delta^{18}O$ in diopside (a proxy for actinolite) from granulite facies marbles, and Kohn (1999) reports similar findings for diopside in amphibolites and pelites. It has also been reported that diffusive exchange of oxygen isotopes during complete granular exsolution of ilmenite from originally Ti-rich magnetite (i.e., where Ti is completely exsolved from magnetite) occurring at variable $f_{(H_2O)}$ during cooling can lower the closure temperature of magnetite and allow for oxygen isotope resetting (Cartwright et al., 1993; Farquhar and Chacko, 1994; Valley, 2001).

The results of the aforementioned studies indicate that the temperatures estimated from the Fe# of actinolite overestimate the temperature of mineralization, and O isotope partitioning between magnetite and actinolite underestimates the temperature of mineralization at Candelaria. Considering the uncertainties inherent in each of the two methods used to estimate temperatures, we suggest that magnetite-actinolite mineralization likely occurred over a temperature range in between the estimations by both methods.

At shallow levels, Marschik and Fontboté (2001a) estimated temperatures of 500° to 600°C for the magnetite-actinolite first stage and ~300° to ~500°C for the Cu-rich second stage at Candelaria, based on fluid inclusions. Pyrite-anhydrite and pyrite-chalcopyrite geothermometry at Candelaria indicates a temperature gradient between 300° and 600°C for the sulfide mineralization through the whole deposit (del Real et al., 2020). Therefore, our estimated temperatures for actinolite and magnetite formation at Candelaria, representing the magnetite-actinolite first stage at deeper levels, are consistent with the temperature differences for sulfide mineralization between shallow and deep (hotter) portions of the system. The temperatures reported here for samples from the deeper zones of Candelaria are also consistent with temperatures reported for IOA deposits. For example, temperatures of 600° to 900°C were reported for massive magnetite mineralization in the Grängesberg mining district, Sweden (Weis, 2013), 610° to >850°C for massive magnetite mineralization at Los Colorados, Chile (Knipping et al., 2015b; Bilenker et al., 2016), up to 840°C at El Romeral, Chile (Rojas et al., 2018), up to 800°C at Cerro Negro Norte, Chile (Salazar et al., 2020), >800°C at el Laco, Chile (Nyström et al., 2008; Tornos et al., 2016), and >800°C for early-stage magnetite at the Gushan deposit, China (Sun et al., 2019). The temperature overlap between the deeper samples from Candelaria and IOA deposits from districts globally provides evidence to support the hypothesis that IOCG mineralization transitions to IOA mineralization with increasing depth.

Additional insight into the temperature(s) of mineralization is provided by the concentrations of trace elements such as Al, Mn, Ti, and V in magnetite, which can be used to assess the temperature of magnetite growth by using the discriminant diagram developed by Nadoll et al. (2014) after Dupuis and Beaudoin (2011). Those authors compiled data for magnetite samples with well-constrained temperatures of formation from ore deposit types that include banded iron formations (BIF), IOCG, IOA, porphyry, and Fe-Ti, V deposits. High-temperature, magmatic, and magmatic-hydrothermal magnetite growth corresponds to samples rich in (Ti + V) and (Al + Mn), whereas low-temperature magnetite growth results in lower concentrations of the same trace elements.

The Al, Mn, Ti, and V concentrations in magnetite from Quince and Candelaria are plotted in Figure 4a. The chemistry of magnetite samples from Quince plot, on average, in the IOA field, and the deeper magnetite samples from Candelaria partially overlap the Quince and shallower Candelaria samples. This suggests that, at depth, the magnetite at Candelaria has a transitional composition between the IOCG and IOA classifications and the temperatures associated with them, which is consistent with the isotope thermometry and actinolite geochemistry previously discussed. The average (Ti + V) and (Al + Mn) values for shallower magnetite samples from Candelaria plot mostly in the IOCG field, with data points extending to higher trace element concentrations that plot in the porphyry and IOA fields and lower trace element concentrations that plot in the BIF field. The shallow Candelaria data yield an average composition that plots on the boundary between IOCG and IOA deposits (Fig. 4a).

Importantly, samples from Quince contain abundant Mn-rich ilmenite exsolution lamellae and interstitial ilmenite, and the deep samples from Candelaria contain Mn-rich ilmenite granules. EPMA analyses were carefully performed to avoid analyzing any exsolved ilmenite lamellae when analyzing magnetite. Similarly, we carefully analyzed interstitial and ilmenite exsolution lamellae to avoid hitting magnetite. The original

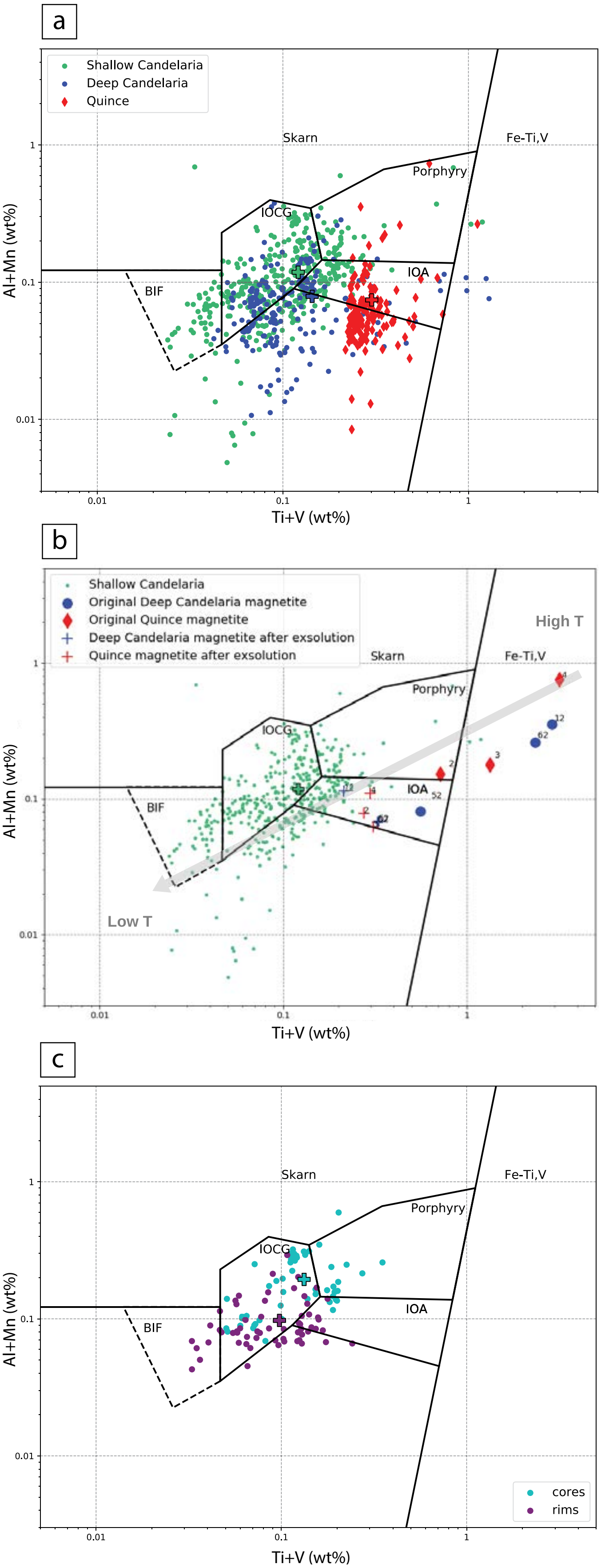

trace element content of magnetite in these samples that now contain exsolved ilmenite was approximated by reintegrating the exsolved ilmenite composition into the host magnetite. The reconstructed original magnetite composition of the deep samples from Candelaria and the samples from Quince plots predominantly in the Fe-Ti, V field (igneous magnetite) (Fig. 4b). This result is consistent with Sun et al. (2019), who reintegrated exsolved ilmenite to calculate the Ti concentration of primary magnetite in the Gushan IOA deposit and report that primary magnetite plots in the Fe-Ti, V field. The originally Ti rich magnetite at Quince and the deep portion of Candelaria is associated with high-temperature formation conditions, as discussed above. When combined with the magnetite chemistry from the Candelaria shallow samples, the data are interpreted to define a cooling trend (Fig. 4b) from the deep to the shallow samples of Candelaria, suggesting that the deep portion of the Candelaria IOCG deposit is chemically analogous to the Quince IOA prospect.

In the zoned magnetite grains (type D) in the shallow part of Candelaria, rims are depleted in Ti, V, Al, and Mn with respect to the cores (Figs. 3b, 4c). This observation is consistent with textures and chemistry from hydrothermal magnetite from the Los Colorados (Knipping et al., 2015b; Deditius et al., 2018) and El Romeral (Rojas et al., 2018) IOA deposits in the Chilean iron belt, and the Pliocene El Laco IOA deposit in northern Chile (Ovalle et al., 2018). Deditius et al. (2018) used transmission electron microscopy (TEM) to identify nanoparticle-sized minerals (diopside, clinoenstatite, amphibole [tremolite-actinolite], phlogopite, ulvöspinel, and Ti-rich magnetite) hosted in the darker areas of zoned, late-stage, low-temperature, hydrothermal magnetite from the Los Colorados IOA deposit. Those authors reported that the magnetite zones that host nanoparticles are also enriched in trace elements and concluded that the nanoparticles formed owing to supersaturation from a hydrothermal fluid, followed by entrapment during continuous

Fig. 4. a) Magnetite discriminant diagram from Nadoll et al. (2014) after Dupuis and Beaudoin (2011). Crosses indicate the average composition for each category. The shallow Candelaria samples (green dots) plot on average in the IOCG field, while the deep Candelaria samples (blue dots) and the Quince samples (red diamonds) plot in the IOA field on average. The partial overlap of the deep Candelaria samples with the shallow Candelaria and the Quince samples suggests a transitional composition and temperature between IOCG and IOA for this part of the system. b) Magnetite discriminant diagram from Nadoll et al. (2014) after Dupuis and Beaudoin (2011). Green dots represent the samples from the shallow part of Candelaria, where the green cross shows their average. Plus signs represent the average trace element concentration of the magnetite samples that contain ilmenite, where blue is for the deep Candelaria samples and red is for Quince samples. Blue circles show the calculated original composition of the magnetite after reintegrating the ilmenite granules at Candelaria, and the red diamonds correspond to the calculated original magnetite from Quince after reintegrating the interstitial ilmenite and the exsolution lamellae. The samples are identified by the number next to the symbol. The arrow is based on the composition-temperature data presented in Nadoll et al. (2014) for the expected trend of the trace element chemistry of magnetite that grows from a cooling magmatic-hydrothermal fluid. c) Magnetite discriminant diagram from Nadoll et al. (2014) after Dupuis and Beaudoin (2011). Dots represent EPMA data from type D magnetite with core to rim zonation in the shallow Candelaria samples. Crosses indicate the average composition for each category. A transition is observed between high-temperature cores enriched in Al, Mn, Ti, and V and low-temperature rims depleted in trace elements.

growth of the magnetite host, similar to our observations for zoned magnetite (type D).

### *Iron and oxygen isotope constraints on the source of ore fluids*

Previous compilations of Fe and O isotope data for igneous settings and different ore deposit types have allowed the determination of ranges of $\delta^{56}$Fe and $\delta^{18}$O that can be associated with particular fluid reservoirs (Taylor, 1967, 1968; Heimann et al., 2008; Jonsson et al., 2013; Weis, 2013; Wawryk and Foden, 2015, 2017; Bilenker et al., 2016; Childress et al., 2016; Troll et al., 2019). The coupled interpretation of Fe-O isotope pairs has proven successful for fingerprinting the provenance of magnetite in IOA deposits worldwide (Weis, 2013; Bilenker et al., 2016; Childress et al., 2016; Troll et al., 2019). All of the $\delta^{56}$Fe and $\delta^{18}$O values from Quince and all but two $\delta^{18}$O values from Candelaria are within the field defined for magmatic/magmatic-hydrothermal magnetite (Fig. 5). A magmatic/magmatic-hydrothermal origin for Fe and O in magnetite from Candelaria is consistent with conclusions based on noble gas and halogen data (Marschik and Kendrick, 2015), fluid-inclusion and stable isotope data, (Marschik and Fontboté, 2001a; del Real et al., 2020), and Re-Os isotope data (Mathur et al., 2002).

[redacted]

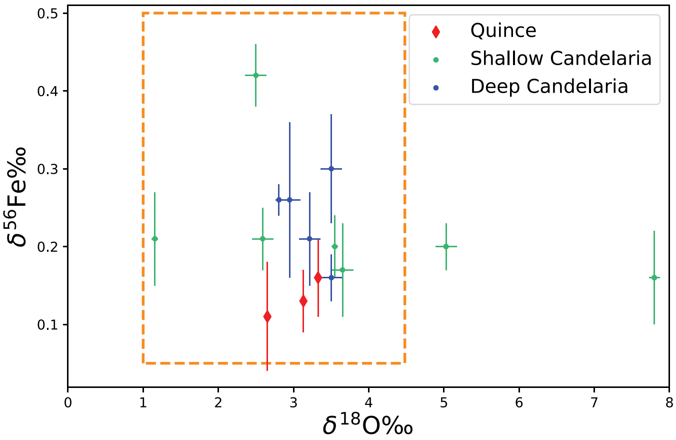

Fig. 5. Magnetite Fe-O isotope pairs for Quince (red) and Candelaria (green = shallow Candelaria; blue = deep Candelaria) with $2\sigma$ error bars. The orange box outlines the range for oxygen (Taylor, 1967, 1968) and iron (Heimann et al, 2008; Bilenker et al., 2016; Troll et al., 2019) isotopes for magmatic and magmatic-hydrothermal magnetite. The two samples that plot outside the magmatic/magmatic-hydrothermal range (orange dashed lines) are discussed in the main text.

[redacted]

Besides fluid-rock interaction, the spread in the $\delta^{18}$O values in the shallow Candelaria samples may reflect redox changes in the system associated with the formation of mushketovite. The increased $\delta^{56}$Fe values at Candelaria with respect to Quince probably reflect a temperature control in the fractionation of Fe isotopes, suggesting that Quince formed at a higher temperature compared to Candelaria.

### *A model that explains IOA and IOCG deposits as part of a genetic continuum*

A genetic link between IOA and IOCG deposits was first hypothesized by Hitzman et al. (1992) based on their global assessment of Proterozoic iron oxide (Cu-U-Au-REE) deposits, and subsequently by Espinoza et al. (1996) based on observations of the spatial and temporal relationships among these classes of deposits in the Chilean iron belt. Our results show that magnetite from the deep portion of the Candelaria IOCG system is very similar—texturally and compositionally—to magnetite from the Quince occurrence (this study) and that the compositions define an interpreted cooling trend in trace element space (Fig. 4b). The compositions of magnetite from Candelaria and Quince are also similar to those reported for the Los Colorados (Knipping et al., 2015a, b), El Romeral (Rojas et al., 2018), and Cerro Negro Norte (Salazar et al., 2020) IOA deposits in the Chilean iron belt and the El Laco IOA deposit in northern Chile (Ovalle et al., 2018). The overlap of magnetite geochemical data for these deposits supports the hypothesized genetic link between IOA and IOCG deposits (Huang and Beaudoin, 2019). A continuum from IOA to IOCG mineralization within individual systems has been suggested for Olympic Dam (Apukhtina et al., 2017), the Great Bear magmatic zone (Corriveau et al., 2016), the Mesoproterozoic St. Francois Mountains terrane, southeast Missouri (Day et al., 2016), and several deposits in the Chilean iron belt (Naslund et al., 2002; Sillitoe, 2003; Barra et al., 2017; Childress et al., 2020).

The observations at Candelaria reveal a clear transition with depth from an IOCG deposit to IOA mineralization (Fig. 6). This is consistent with the genetic model proposed by Knipping et al. (2015a) that explains IOCG and IOA mineralization as parts of a single continuum resulting from the combination of igneous and magmatic-hydrothermal processes. In their unifying model, microlites of Ti-rich magnetite (i.e., type A with inclusions and type B with exsolved ilmenite) crystallize from a silicate melt and serve as nucleation sites for magmatic-hydrothermal fluid that is exsolved from silicate melt during decompression. Continued degassing of magmatic-hydrothermal fluid that nucleates as bubbles on magnetite microlites results in the formation of a magnetite-fluid suspension that is more buoyant than the surrounding magma, allowing this magnetite-bearing ore fluid to ascend and carry Ti-rich magnetite (Knipping et al., 2019). During ascent and emplacement, the ore fluid will react with Ti-rich magnetite, promoting local dissolution-reprecipitation reactions along grain boundaries, catalyzing the exsolution of Ti from the lamellae into ilmenite granules (Buddington and Lindsley, 1964), and precipitating exsolution- and inclusion-free magnetite (type C). The presence of triple junctions among magnetite grains, as well as the trace element zonation between cores and rims within single grains, preserves evidence for such processes. Experimental data (Hezarkhani et al., 1999; Ulrich et al., 2001; Hurtig and Williams-Jones, 2014; Williams-Jones and Migdisov, 2014) demonstrate that the exsolved magmatic-hydrothermal fluid continues to transport Fe, Cu, Au, and S after forming IOA mineralization at depth. The fluid continues to cool during ascent and precipitates oxides and sulfides in the shallower levels of the system to form an IOCG deposit (Knipping et al., 2015a; Reich et al., 2016; Simon et al., 2018). Type D magnetite and mushketovite, which are only present in the shallow zone of Candelaria, are purely hydrothermal minerals that precipitated from the ascending fluid after it produced IOA mineralization at deeper levels of the system. Marschik and Fontboté (2001a) report that type D magnetite precipitated at temperatures between 500° and 600°C and was followed by chalcopyrite and pyrite mineralization as the fluid cooled below 500°C.

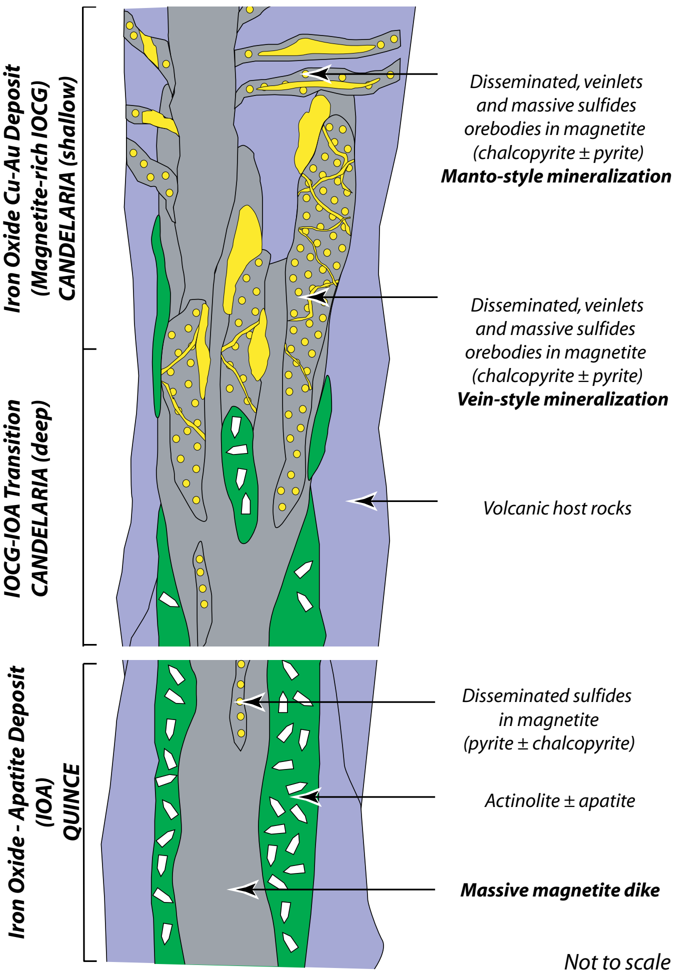

Fig. 6. Schematic representation of the IOA-IOCG continuum and characteristic mineralization of each section, where Quince is the IOA mineral deposit, shallow Candelaria is the IOCG mineral deposit, and deep Candelaria represents the transition between both. (Modified from Barra et al., 2017.)

## Conclusions

The Fe and O stable isotope data for magnetite and H isotope data for actinolite support a magmatic/magmatic-hydrothermal origin for the Candelaria IOCG and the Quince IOA mineral deposits in the Chilean iron belt. The trellis and cloth textures, triple junctions, and zonation in magnetite grains are consistent with oxyexsolution of a primary magnetite-ulvöspinel solid solution to magnetite that contains ilmenite exsolution lamellae. This process was enhanced by syn- or post-mineralization dissolution-reprecipitation and reequilibration processes of originally Ti rich magnetite caused by the interaction with a cooling hypogene magmatic-hydrothermal fluid. Such interaction is also reflected in the geochemical zonation of trace elements, which systematically decrease from core to rim in individual (zoned) magnetite grains and between deep and shallow samples.

The geochemical and textural characterization of magnetite and actinolite from Candelaria and Quince indicates a magmatic to magmatic-hydrothermal origin for these mineral deposits and suggests that the deep part of Candelaria represents the transition between shallow IOCG and deeper IOA mineralization. The flotation model, as proposed by Knipping et al. (2015a), can explain the origin of both Quince and Candelaria, supporting the hypothesis that IOA and IOCG deposits are parts of a single genetic continuum.

## Acknowledgments

MARM thanks the Society of Economic Geologists and the University of Michigan for providing funding. ACS acknowledges funding from National Science Foundation Earth Sciences (NSF EAR) grants 1924142, 1250239, and 1264560. FB acknowledges funding from Chile's Millennium Science Initiative (MSI) through Millennium Nucleus for Metal Tracing Along Subduction, and from Fondo Nacional de Desarrollo Científico y Tecnológico (FONDECYT) grant 1140780 "Metallogenesis of the Mesozoic magmatic arc of northern Chile: Testing the IOCG connection using a multi-proxy geochemical approach." IB acknowledges support from NSF EAR grant 1822977. The authors thank Dominique Weis for access to the Pacific Center for Isotopic and Geochemical Research (PCIGR) labs at the University of British Columbia, Lundin Mining for providing access to Candelaria, and reviewers Lena Virgínia Soares Monteiro and Olof Martinsson and Editor Larry Meinert for their comments, which helped improve this manuscript.

## REFERENCES

Apukhtina, O.B., Kamenetsky, V.S., Ehrig, K., Kamenetsky, M.B., Maas, R., Thompson, J., McPhie, J., Ciobanu, C.L., and Cook, N.J., 2017, Early, deep magnetite-fluorapatite mineralization at the Olympic Dam Cu-U-Au-Ag deposit, South Australia: Economic Geology, v. 112, p. 1531–1542.

Arguin, J.-P., Pagé, P., Barnes, S.-J., Girard, R., and Duran, C., 2018, An integrated model for ilmenite, Al-spinel, and corundum exsolutions in titanomagnetite from oxide-rich layers of the Lac Doré Complex (Québec, Canada): Minerals, v. 8, article 476, 39 p.

Barra, F., Reich, M., Selby, D., Rojas, P., Simon, A., Salazar, E., and Palma, G., 2017, Unraveling the origin of the Andean IOCG clan: A Re-Os isotope approach: Ore Geology Reviews, v. 81, p. 62–78.

Barton, M.D., 2014, Iron oxide(-Cu-Au-REE-P-Ag-U-Co) systems, *in* Holland, H.D., and Turekian, K.K., eds., Treatise on geochemistry, 2nd ed.: Oxford, Elsevier, p. 515–541.

Barton, M.D., and Johnson, D.A., 1996, An evaporitic-source model for igneous-related Fe oxide(-REE-Cu-Au-U) mineralization: Geology, v. 24, p. 259–262.

Benavides, J., Kyser, T.K., Clark, A.H., Oates, C.J., Zamora, R., Tarnovschi, R., and Castillo, B., 2007, The Mantoverde iron oxide-copper-gold district, III Región, Chile: The role of regionally derived, nonmagmatic fluids in chalcopyrite mineralization: Economic Geology, v. 102, p. 415–440.

Bilenker, L.D., Simon, A.C., Reich, M., Lundstrom, C.C., Gajos, N., Bindeman, I., Barra, F., and Munizaga, R., 2016, Fe-O stable isotope pairs elucidate a high-temperature origin of Chilean iron oxide-apatite deposits: Geochimica et Cosmochimica Acta, v. 177, p. 94–104.

Bindeman, I.N., Kamenetsky, V.S., Palandri, J., and Vennemann, T., 2012, Hydrogen and oxygen isotope behaviors during variable degrees of upper mantle melting: Example from the basaltic glasses from Macquarie Island: Chemical Geology, v. 310–311, p. 126–136, doi: 10.1016/j.chemgeo.2012.03.031.

Brown, M., Diáz, F., and Grocott, J., 1993, Displacement history of the Atacama fault system 25°00′S-27° 00′S, northern Chile: Geological Society of America (GSA) Bulletin, v. 105, p. 1165–1174.

Buddington, A.F., and Lindsley, D.H., 1964, Iron-titanium oxide minerals and synthetic equivalents: Journal of Petrology, v. 5, p. 310–357.

Carmichael, I.S.E., 1966, The iron-titanium oxides of salic volcanic rocks and their associated ferromagnesian silicates: Contributions to Mineralogy and Petrology, v. 14, p. 36–64.

Cartwright, I., Valley, J.W., and Hazelwood, A.-M., 1993, Resetting of oxybarometers and oxygen isotope ratios in granulite facies orthogneisses during cooling and shearing, Adirondack Mountains, New York: Contributions to Mineralogy and Petrology, v. 113, p. 208–225.

Charrier, R., Pinto, L., and Rodríguez, M.P., 2007, Tectonostratigraphic evolution of the Andean orogen in Chile, *in* Moreno, T., and Gibbons, W., eds., The geology of Chile: London, Geological Society of London, p. 21–114.

Chen, H., Kyser, T.K., and Clark, A.H., 2011, Contrasting fluids and reservoirs in the contiguous Marcona and Mina Justa iron oxide-Cu (-Ag-Au) deposits, south-central Perú: Mineralium Deposita, v. 46, p. 677–706.

Chiaradia, M., Banks, D., Cliff, R., Marschik, R., and de Haller, A., 2006, Origin of fluids in iron oxide-copper-gold deposits: Constraints from $\delta^{37}$Cl, $^{87}$Sr/$^{86}$Sr$_i$ and Cl/Br: Mineralium Deposita, v. 41, p. 565–573.

Chiba, H., Chacko, T., Clayton, R.N., and Goldsmith, J.R., 1989, Oxygen isotope fractionations involving diopside, forsterite, magnetite, and calcite: Application to geothermometry: Geochimica et Cosmochimica Acta, v. 53, p. 2985–2995.

Childress, T.M., Simon, A.C., Day, W.C., Lundstrom, C.C., and Bindeman, I.N., 2016, Iron and oxygen isotope signatures of the Pea Ridge and Pilot Knob magnetite-apatite deposits, southeast Missouri, USA: Economic Geology, v. 111, p. 2033–2044.

Childress, T.M., Simon, A.C., Reich, M., Barra, F., Arce, M., Lundstrom, C.C., and Bindeman, I.N., 2020, Formation of the Mantoverde iron oxide-copper-gold (IOCG) deposit, Chile: Insights from Fe and O stable isotopes and comparisons with iron oxide-apatite (IOA) deposits: Mineralium Deposita, doi: 10.1007/s00126-019-00936-x.

Corriveau, L., Montreuil, J.-F., and Potter, E.G., 2016, Alteration facies linkages among iron oxide copper-gold, iron oxide-apatite, and affiliated deposits in the Great Bear magmatic zone, Northwest Territories, Canada: Economic Geology, v. 111, p. 2045–2072.

Couture, J.-F., Cole, G., Zhang, B., Scott, C.C., Kautzman, S., Nilsson, J., Dance, A., and Vidal, M.I., 2018, Technical Report for the Candelaria Copper mining complex, Atacama region, Region III, Chile: SRK Consulting 3CL014.002, www.lundinmining.com/site/assets/files/3641/candelaria_2018_tr.pdf, accessed January 15, 2019.

Craddock, P.R., and Dauphas, N., 2011, Iron isotopic compositions of geological reference materials and chondrites: Geostandards and Geoanalytical Research, v. 35, p. 101–123.

Day, W.C., Slack, J.F., Ayuso, R.A., and Seeger, C.M., 2016, Regional geologic and petrologic framework for iron oxide ± apatite ± rare earth element and iron oxide copper-gold deposits of the Mesoproterozoic St. Francois Mountains terrane, southeast Missouri, USA: Economic Geology, v. 111, p. 1825–1858.

Deditius, A.P., Reich, M., Simon, A.C., Suvorova, A., Knipping, J., Roberts, M.P., Rubanov, S., Dodd, A., and Saunders, M., 2018, Nanogeochemistry of hydrothermal magnetite: Contributions to Mineralogy and Petrology, v. 173, article 46.

del Real, I., Thompson, J.F.H., and Carriedo, J., 2018, Lithological and structural controls on the genesis of the Candelaria-Punta del Cobre iron oxide copper gold district, Northern Chile: Ore Geology Reviews, v. 102, p. 106–153.

del Real, I., Thompson, J.F.H., Simon, A.C., and Reich, M., 2020, Geochemical and isotopic signature of pyrite as a proxy for fluid source and evolution in the Candelaria-Punta del Cobre iron oxide copper-gold district, Chile: Economic Geology, v. 115, p. 1493–1517.

Dupuis, C., and Beaudoin, G., 2011, Discriminant diagrams for iron oxide trace element fingerprinting of mineral deposit types: Mineralium Deposita, v. 46, p. 319–335.

Edwards, K.J., and Valley, J.W., 1998, Oxygen isotope diffusion and zoning in diopside: The importance of water fugacity during cooling: Geochimica et Cosmochimica Acta, v. 62, p. 2265–2277.

Espinoza, S., Veliz, H., Esquivel, J., Arias, J., and Moraga, A., 1996, The cupriferous province of the Coastal Range, Northern Chile: Society of Economic Geologists, Special Publication 5, p. 19–32.

Farquhar, J., and Chacko, T., 1994, Exsolution-enhanced oxygen exchange: Implications for oxygen isotope closure temperatures in minerals: Geology, v. 22, p. 751–754.

Farquhar, J., Chacko, T., and Frost, B.R., 1993, Strategies for high-temperature oxygen isotope thermometry: A worked example from the Laramie Anorthosite Complex, Wyoming, USA: Earth and Planetary Science Letters, v. 117, p. 407–422.

Groves, D.I., Bierlein, F.P., Meinert, L.D., and Hitzman, M.W., 2010, Iron oxide copper-gold (IOCG) deposits through Earth history: Implications for origin, lithospheric setting, and distinction from other epigenetic iron oxide deposits: Economic Geology, v. 105, p. 641–654.

Gruenewaldt, G.V., Klemm, D.D., Henckel, J., and Dehm, R.M., 1985, Exsolution features in titanomagnetites from massive magnetite layers and their host rocks of the upper zone, eastern Bushveld Complex: Economic Geology, v. 80, p. 1049–1061.

Haggerty, S., 1976, Opaque mineral oxides in terrestrial igneous rocks: Mineralogical Society of America, Short Course Notes, v. 3, p. 101–300.

Haynes, D.W., 2000, Iron oxide copper (-gold) deposits: Their position in the ore spectrum and modes of origin, *in* Porter, T.M., ed., Hydrothermal iron oxide copper-gold and related deposits: A global perspective: Adelaide, PGC Publishing, p. 71–90.

Hedenquist, J.W., and Lowenstern, J.B., 1994, The role of magmas in the formation of hydrothermal ore deposits: Nature, v. 370, p. 519–527.

Heidarian, H., Lentz, D., Alirezaei, S., Peighambari, S., and Hall, D., 2016, Using the chemical analysis of magnetite to constrain various stages in the formation and genesis of the Kiruna-type Chadormalu magnetite-apatite deposit, Bafq district, central Iran: Mineralogy and Petrology, v. 110, p. 927–942.

Heimann, A., Beard, B.L., and Johnson, C.M., 2008, The role of volatile exsolution and sub-solidus fluid/rock interactions in producing high $^{56}$Fe/$^{54}$Fe ratios in siliceous igneous rocks: Geochimica et Cosmochimica Acta, v. 72, p. 4379–4396.

Hezarkhani, A., Williams-Jones, A.E., and Gammons, C.H., 1999, Factors controlling copper solubility and chalcopyrite deposition in the Sungun porphyry copper deposit, Iran: Mineralium Deposita, v. 34, p. 770–783.

Hildebrand, R.S., 1986, Kiruna-type deposits; their origin and relationship to intermediate subvolcanic plutons in the Great Bear magmatic zone, northwest Canada: Economic Geology, v. 81, p. 640–659.

Hitzman, M.W., 2000, Iron oxide-Cu-Au deposits: What, where, when, and why, *in* Porter, T.M., ed., Hydrothermal iron oxide copper-gold and related deposits: A global perspective, v. 1: Adelaide, PGC Publishing, p. 9–25.

Hitzman, M.W., Oreskes, N., and Einaudi, M.T., 1992, Geological characteristics and tectonic setting of Proterozoic iron oxide (Cu-U-Au-REE) deposits: Precambrian Research, v. 58, p. 241–287.

Hou, T., Charlier, B., and Namur, O., 2018, Immiscible hydrous Fe-Ca-P melt and the origin of iron oxide-apatite ore deposits: Nature Communications, v. 9, p. 1–8.

Hu, H., Li, J.-W., Lentz, D., Ren, Z., Zhao, X.-F., Deng, X.-D., and Hall, D., 2014, Dissolution-reprecipitation process of magnetite from the Chengchao iron deposit: Insights into ore genesis and implication for in-situ chemical analysis of magnetite: Ore Geology Reviews, v. 57, p. 393–405.

Huang, F., Zhang, Z., Lundstrom, C.C., and Zhi, X., 2011, Iron and magnesium isotopic compositions of peridotite xenoliths from eastern China: Geochimica et Cosmochimica Acta, v. 75, p. 3318–3334.

Huang, X.-W., and Beaudoin, G., 2019, Textures and chemical compositions of magnetite from iron oxide copper-gold (IOCG) and Kiruna-type iron oxide-apatite (IOA) deposits and their implications for ore genesis and magnetite classification schemes: Economic Geology, v. 114, p. 953–979.

Hurtig, N.C., and Williams-Jones, A.E., 2014, An experimental study of the transport of gold through hydration of AuCl in aqueous vapour and vapour-like fluids: Geochimica et Cosmochimica Acta, v. 127, p. 305–325.

Jonsson, E., Troll, V.R., Högdahl, K., Harris, C., Weis, F., Nilsson, K.P., and Skelton, A., 2013, Magmatic origin of giant "Kiruna-type" apatite-iron-oxide ores in central Sweden: Scientific Reports, v. 3, p. 1–8.

Knipping, J.L., Bilenker, L.D., Simon, A.C., Reich, M., Barra, F., Deditius, A.P., Lundstrom, C., Bindeman, I., and Munizaga, R., 2015a, Giant Kiruna-type deposits form by efficient flotation of magmatic magnetite suspensions: Geology, v. 43, p. 591–594.

Knipping, J.L., Bilenker, L.D., Simon, A.C., Reich, M., Barra, F., Deditius, A.P., Wälle, M., Heinrich, C.A., Holtz, F., and Munizaga, R., 2015b, Trace elements in magnetite from massive iron oxide-apatite deposits indicate a combined formation by igneous and magmatic-hydrothermal processes: Geochimica et Cosmochimica Acta, v. 171, p. 15–38.

Knipping, J.L., Webster, J.D., Simon, A.C., and Holtz, F., 2019, Accumulation of magnetite by flotation on bubbles during decompression of silicate magma: Scientific Reports, v. 9, article 3852.

Kohn, M.J., 1999, Why most dry rocks should cool wet: American Mineralogist, v. 84, p. 570–580.

Lledo, H.L., and Jenkins, D.M., 2008, Experimental investigation of the upper thermal stability of Mg-rich actinolite; implications for Kiruna-type iron deposits: Journal of Petrology, v. 49, no. 2, p. 225–238.

Loewen, M.W., and Bindeman, I.N., 2016, Oxygen isotope thermometry reveals high magmatic temperatures and short residence times in Yellowstone and other hot-dry rhyolites compared to cold-wet systems: American Mineralogist, v. 101, p. 1222–1227.

Lund, C., 2013, Mineralogical, chemical and textural characterisation of the Malmberget iron ore deposit for a geometallurgical model: Ph.D. thesis, Sweden, Lulea University of Technology, 188 p.

Mark, G., and Foster, D.R.W., 2000, Magmatic-hydrothermal albite-actinolite-apatite-rich rocks from the Cloncurry district, NW Queensland, Australia: Lithos, v. 51, no. 3, p. 223–245, doi: 10.1016/S0024-4937(99)00069-9.

Marschik, R., and Fontboté, L., 2001a, The Candelaria-Punta del Cobre iron oxide Cu-Au(-Zn-Ag) deposits, Chile: Economic Geology, v. 96, p. 1799–1826.

——2001b, The Punta del Cobre Formation, Punta del Cobre-Candelaria area, northern Chile: Journal of South American Earth Sciences, v. 14, p. 401–433.

Marschik, R., and Kendrick, M.A., 2015, Noble gas and halogen constraints on fluid sources in iron oxide-copper-gold mineralization: Mantoverde and La Candelaria, northern Chile: Mineralium Deposita, v. 50, p. 357–371.

Marschik, R., Singer, B.S., Munizaga, F., Tassinari, C., Moritz, R., and Fontboté, L., 1997, Age of Cu(-Fe)-Au mineralization and thermal evolution of the Punta del Cobre district, Chile: Mineralium Deposita, v. 32, p. 531–546.

Marschik, R., Leveille, R.A., and Martin, W., 2000, La Candelaria and the Punta del Cobre district, Chile: Early Cretaceous iron oxide Cu-Au-Zn-Ag) mineralization, *in* Porter, T.M., ed., Hydrothermal iron-oxide copper-gold and related deposits: A global perspective: Adelaide, Australian Mineral Foundation, p. 163–175.

Mathur, R., Marschik, R., Ruiz, J., Munizaga, F., Leveille, R., and Martin, W., 2002, Age of mineralization of the Candelaria Fe oxide Cu-Au deposit and the origin of the Chilean iron belt, based on Re-Os isotopes: Economic Geology, v. 97, p. 59–71.

Ménard, J.-J., 1995, Relationship between altered pyroxene diorite and the magnetite mineralization in the Chilean iron belt, with emphasis on the El Algarrobo iron deposits (Atacama region, Chile): Mineralium Deposita, v. 30, p. 268–274.

Mourgues, F.A., 2004, Advances in ammonite biostratigraphy of the marine Atacama basin (Lower Cretaceous), northern Chile, and its relationship with the Neuquén basin, Argentina: Journal of South American Earth Sciences, v. 17, p. 3–10.

Nadoll, P., Angerer, T., Mauk, J.L., French, D., and Walshe, J., 2014, The chemistry of hydrothermal magnetite: A review: Ore Geology Reviews, v. 61, p. 1–32.

Naslund, H.R., Henriquez, F., Nyström, J.O., Vivallo, W., and Dobbs, F.M., 2002, Magmatic iron ores and associated mineralisation: Examples from the Chilean High Andes and Coastal Cordillera, *in* Porter, T.M. ed., Hydrothermal iron oxide copper-gold and related deposits: A global perspective, v. 2: Adelaide, PGC Publishing, p. 207–226.

Neybergh, H., Laduron, D., Martin, H., and Verkaeren, J., 1980, The vanadiferous magnetite deposits of the Oursi region, Upper-Volta: Economic Geology, v. 75, p. 1042–1052.

Nyström, J.O., and Henriquez, F., 1994, Magmatic features of iron ores of the Kiruna type in Chile and Sweden; ore textures and magnetite geochemistry: Economic Geology, v. 89, p. 820–839.

Nyström, J.O., Billström, K., Henríquez, F., Fallick, A.E., and Naslund, H.R., 2008, Oxygen isotope composition of magnetite in iron ores of the Kiruna type in Chile and Sweden: Journal of the Geological Society of Sweden (GFF), v. 130, p. 177–188.

Ovalle, J.T., La Cruz, N.L., Reich, M., Barra, F., Simon, A.C., Konecke, B.A., Rodriguez-Mustafa, M.A., Deditius, A.P., Childress, T.M., and Morata, D., 2018, Formation of massive iron deposits linked to explosive volcanic eruptions: Scientific Reports, v. 8, article 14855.

Palma, G., Barra, F., Reich, M., Valencia, V., Simon, A.C., Vervoort, J., Leisen, M., and Romero, R., 2019, Halogens, trace element concentrations, and Sr-Nd isotopes in apatite from iron oxide-apatite (IOA) deposits in the Chilean iron belt: Evidence for magmatic and hydrothermal stages of mineralization: Geochimica et Cosmochimica Acta, v. 246, p. 515–540.

Pang, K.-N., Zhou, M.-F., Lindsley, D., Zhao, D., and Malpas, J., 2008, Origin of Fe-Ti oxide ores in mafic intrusions: Evidence from the Panzhihua intrusion, SW China: Journal of Petrology, v. 49, p. 295–313.

Pollard, P.J., 2006, An intrusion-related origin for Cu-Au mineralization in iron oxide-copper-gold (IOCG) provinces: Mineralium Deposita, v. 41, p. 179–187.

Price, G.D., Dashwood, B., Taylor, G.K., Kalin, R.M., and Ogle, N., 2008, Carbon isotope and magnetostratigraphy of the Cretaceous (Barremian-Aptian) Pabellón Formation, Chañarcillo basin, Chile: Cretaceous Research, v. 29, p. 183–191.

Qi, H., Coplen, T.B., Gehre, M., Vennemann, T.W., Brand, W.A., Geilmann, H., Olack, G., Bindeman, I.N., Palandri, J., Huang, L., and Longstaffe, F.J., 2017, New biotite and muscovite isotopic reference materials, USGS57 and USGS58, for $\delta^2$H measurements—a replacement for NBS 30: Chemical Geology, v. 467, p. 89–99.

Quince Iron Chile, 2019, www.quinceironchile.com/.

Rabbia, O.M., and Hernández, L.B., 2012, Mineral chemistry and potential applications of natural-multi-doped hydrothermal rutile from porphyry copper deposits, *in* Low, I.-M., ed., Rutile: Properties, synthesis and applications: New York, Nova Science Publishers, Inc., p. 209–228.

Rabbia, O.M., Hernández, L.B., French, D.H., King, R.W., and Ayers, J.C., 2009, The El Teniente porphyry Cu-Mo deposit from a hydrothermal rutile perspective: Mineralium Deposita, v. 44, p. 849–866.

Reich, M., Simon, A.C., Deditius, A.P., Barra, F., Chryssoulis, S., Lagas, G., Tardani, D., Knipping, J., Bilenker, L., Sánchez-Alfaro, P., Roberts, M.P., and Munizaga, R., 2016, Trace element signature of pyrite from the Los Colorados iron oxide-apatite (IOA) deposit, Chile: A missing link between Andean IOA and IOCG Systems?: Economic Geology, v. 111, p. 743–761.

Rhodes, A., and Oreskes, N., 1999, Oxygen isotope composition of magnetite deposits at El Laco, Chile: Evidence of formation from isotopically heavy fluids: Society of Economic Geologists, Special Publication, 7, p. 333–351.

Rieger, A.A., and Marschik, R., 2012, The evolution of the hydrothermal IOCG system in the Mantoverde district, northern Chile: New evidence from microthermometry and stable isotope geochemistry: Mineralium Deposita, v. 47, p. 359–369.

Rojas, P.A., Barra, F., Deditius, A., Reich, M., Simon, A., Roberts, M., and Rojo, M., 2018, New contributions to the understanding of Kiruna-type iron oxide-apatite deposits revealed by magnetite ore and gangue mineral geochemistry at the El Romeral deposit, Chile: Ore Geology Reviews, v. 93, p. 413–435.

Salazar, E., Barra, F., Reich, M., Simon, A., Leisen, M., Palma, G., Romero, R., and Rojo, M., 2020, Trace element geochemistry of magnetite from the Cerro Negro Norte iron oxide-apatite deposit, northern Chile: Mineralium Deposita, v. 55, p. 409–428.

Sillitoe, R.H., 2003, Iron oxide-copper-gold deposits: An Andean view: Mineralium Deposita, v. 38, p. 787–812.

Simon, A., Knipping, J., Reich, M., Barra, F., Deditius, A., Bilenker, L., and Childress, T., 2018, A holistic model that combines igneous and magmatic-hydrothermal processes to explain Kiruna-type iron oxide-apatite deposits and iron oxide-copper-gold deposits as products of a single evolving ore system: Society of Economic Geologists, Special Publication 21, p. 89–114.

SRK Consulting, 2014, Quince Sur iron project preliminary economic assessment: Report 05-2501-11, p. 11–31.

Sun, W., Yuan, F., Jowitt, S.M., Zhou, T., Liu, G., Li, X., Wang, F., and Troll, V.R., 2019, In situ LA-ICP-MS trace element analyses of magnetite: Genetic implications for the Zhonggu orefield, Ningwu volcanic basin, Anhui Province, China: Mineralium Deposita, v. 54, p. 1243–1264.

Tan, W., Liu, P., He, H., Wang, C.Y., and Liang, X., 2016, Mineralogy and origin of exsolution in Ti-rich magnetite from different magmatic Fe-Ti oxide-bearing intrusions: The Canadian Mineralogist, v. 54, p. 539–553.

Taylor, H.P., 1967, Oxygen isotope studies of hydrothermal mineral deposits, *in* Barnes, H.L., ed., Geochemistry of hydrothermal ore deposits: New York, Holt, Rinehart and Winston, p. 109–142.

——1968, The oxygen isotope geochemistry of igneous rocks: Contributions to Mineralogy and Petrology, v. 19, p. 1–71.

——1974, The application of oxygen and hydrogen isotope studies to problems of hydrothermal alteration and ore deposition: Economic Geology, v. 69, p. 843–883.

Tornos, F., Velasco, F., and Hanchar, J.M., 2016, Iron-rich melts, magmatic magnetite, and superheated hydrothermal systems: The El Laco deposit, Chile: Geology, v. 44, p. 427–430.

Tornos, F., Velasco, F., and Hanchar, J.M., 2017, The magmatic to magmatic-hydrothermal evolution of the El Laco deposit (Chile) and its implications for the genesis of magnetite-apatite deposits: Economic Geology, v. 112, p. 1595–1628.

Troll, V.R., Weis, F.A., Jonsson, E., Andersson, U.B., Majidi, S.A., Högdahl, K., Harris, C., Millet, M.-A., Chinnasamy, S.S., Kooijman, E., and Nilsson, K.P., 2019, Global Fe-O isotope correlation reveals magmatic origin of Kiruna-type apatite-iron-oxide ores: Nature Communications, v. 10, article 1712.

Ulrich, T., Günther, D., and Heinrich, C.A., 2001, The evolution of a porphyry Cu-Au deposit, based on LA-ICP-MS analysis of fluid inclusions: Bajo de la Alumbrera, Argentina: Economic Geology, v. 96, p. 1743–1774.

Valley, J.W., 2001, Stable isotope thermometry at high temperatures: Reviews in Mineralogy and Geochemistry, v. 43, p. 365–413.

Veloso, E., Cembrano, J., Arancibia, G., Heuser, G., Neira, S., Siña, A., Garrido, I., Vermeesch, P., and Selby, D., 2017, Tectono-metallogenetic evolution of the Fe-Cu deposit of Dominga, northern Chile: Mineralium Deposita, v. 52, p. 595–620.

Wawryk, C.M., and Foden, J.D., 2015, Fe-isotope fractionation in magmatic-hydrothermal mineral deposits: A case study from the Renison Sn-W deposit, Tasmania: Geochimica et Cosmochimica Acta, v. 150, p. 285–298.

——2017, Iron-isotope systematics from the Batu Hijau Cu-Au deposit, Sumbawa, Indonesia: Chemical Geology, v. 466, p. 159–172.

Weis, F., 2013, Oxygen and iron isotope systematics of the Grängesberg mining district (GMD), central Sweden: Ph.D. dissertation, Sweden, Uppsala University, p. 1–83.

Westhues, A., Hanchar, J.M., LeMessurier, M.J., and Whitehouse, M.J., 2017a, Evidence for hydrothermal alteration and source regions for the Kiruna iron oxide-apatite ore (northern Sweden) from zircon Hf and O isotopes: Geology, v. 45, p. 571–574.

Westhues, A., Hanchar, J.M., Voisey, C.R., Whitehouse, M.J., Rossman, G.R., and Wirth, R., 2017b, Tracing the fluid evolution of the Kiruna iron oxide apatite deposits using zircon, monazite, and whole rock trace elements and isotopic studies: Chemical Geology, v. 466, p. 303–322.

Williams, P., Barton, M.D., Johnson, D.A., Fontboté, L., De Haller, A., Mark, G., Oliver, N.H.S., and Marschik, R., 2005, Iron oxide copper-gold deposits: Geology, space-time distribution, and possible modes of origin: Economic Geology 100th Anniversary Volume, p. 371–405.

Williams-Jones, A.E., and Migdisov, A.A., 2014, Experimental constraints on the transport and deposition of metals in ore-forming hydrothermal systems: Society of Economic Geologists, Special Publication 18, p. 77–95.

**Maria Alejandra Rodriguez-Mustafa** is a Ph.D. candidate at the University of Michigan investigating the origin of iron oxide copper-gold (IOCG) and iron oxide-apatite (IOA) ore deposits. Maria earned her B.S. Honors degree in geology from the National University of Colombia.